



# Rovibrational dynamics of the quasistructural N<sub>2</sub> dimer



Roland Tóbiás <sup>1,2</sup> , Csaba Fábián <sup>3</sup>, Marlene Bosquez <sup>1,4</sup>, Monika Kodrycka <sup>5</sup>, Konrad Patkowski <sup>5</sup> & Attila G. Császár <sup>1</sup>

Although the collision-induced absorption spectrum of the nitrogen gas is known in considerable detail, little has been learned experimentally about the structural, dynamical, and rovibrational characteristics of the nitrogen dimer itself. This study explores all these properties of this prototypical van der Waals (vdW) dimer and provides definitive quantum chemical results, mostly with attached conservative uncertainty estimates, particularly for the parent isotopologue, <sup>14</sup>N<sub>2</sub>·<sup>14</sup>N<sub>2</sub>. The results obtained are based on three analytical representations of the dimer's ground-state potential energy surface (PES), including two full-dimensional models of spectroscopic accuracy, constructed during the present study. The structural and focal-point analyses confirm that the global minimum of (N<sub>2</sub>)<sub>2</sub> is planar and has a tilted, Z-shaped form, with an electronic dissociation energy of 109.3(26) cm<sup>-1</sup>. After considering zero-point vibrational effects variationally, the first dissociation limit of <sup>14</sup>N<sub>2</sub>·<sup>14</sup>N<sub>2</sub> is estimated to be 72.2(15) cm<sup>-1</sup>. The full- and reduced-dimensional variational nuclear-motion computations performed result in almost 6000 bound rovibrational states for <sup>14</sup>N<sub>2</sub>·<sup>14</sup>N<sub>2</sub>, including over 100 purely vibrational modes. Effects arising from isotopic substitutions, as well as the shifts and splittings of the two quasi-bound N ≡ N stretch fundamentals, are also examined. An in-depth analysis of the rovibrational eigenstates indicates that N<sub>2</sub>·N<sub>2</sub> is a quasistructural molecular complex.

Nitrogen gas is one of the principal atmospheric constituents not only on Earth, but also on exoplanets, moons, and even certain stars. As the parent isotopologue of the diatomic N<sub>2</sub> molecule, <sup>14</sup>N<sub>2</sub>, has no intrinsic dipole moment, its typical rovibrational spectral features are due to its nonzero quadrupole moment<sup>1,2</sup>. At a sufficiently high pressure, broad spectral features in the infrared region of the electromagnetic spectrum have been observed<sup>3,4</sup> for molecules lacking permanent dipole moments, like H<sub>2</sub>, N<sub>2</sub>, O<sub>2</sub>, CH<sub>4</sub>, and their mixtures. At lower gas densities, these features are basically due to binary collisions governed by subtle non-covalent interactions (NCI)<sup>5,6</sup>, resulting in what are called collision-induced absorption (CIA) spectra<sup>7</sup>. For N<sub>2</sub>·N<sub>2</sub>, the collision-induced dipole arises from the polarization of one monomer by the quadrupolar field of the other one.

The CIA spectrum of the nitrogen gas was discovered in the laboratory in 1949<sup>3</sup>. This observation was followed by numerous experimental<sup>8–24</sup> and theoretical/computational<sup>25–28</sup> investigations. In particular, CIA spectra of the nitrogen gas have been measured both in the Earth's atmosphere<sup>20</sup> and in that of Saturn's largest moon, Titan<sup>11,19</sup>. At low N<sub>2</sub> concentrations, it is hard to record the CIA spectrum<sup>3,18</sup>, but it becomes much more visible in

nitrogen-rich atmospheres, such as that of Earth. CIA even contributes to a small extent to the natural greenhouse effect<sup>20</sup>. It is worth mentioning that the CIA of the nitrogen gas had to be accounted for to explain that the atmosphere of early Mars was warm enough to support liquid water on its surface<sup>29</sup>.

Starting from its 2012 edition<sup>30</sup>, the canonical spectroscopic database HITRAN provides CIA-related parameters<sup>22,30</sup>. They are available for 20 binary systems in its latest version, HITRAN2020<sup>31</sup>, listed separately from the more usual line-by-line spectroscopic data. For the N<sub>2</sub> dimer, there are more than 250000 CIA coefficients, collected from both experimental<sup>13,16,17,21</sup> and theoretical/computational<sup>23,27,28</sup> data sources, in diverse temperature ranges between 70 and 400 K. These data span the 0–650, 1850–3000, and 4300–5000 cm<sup>-1</sup> spectral regions. The first wavenumber range contains the intermonomer vibrational bands of the N<sub>2</sub> dimer, while the second and third intervals cover transitions involving the two intramonomer (N ≡ N stretch) fundamentals and their first overtones, respectively. Some of these CIA coefficients may have limited accuracy, due to (a) experimental uncertainties, often caused by ill-resolved overlapping lines and/or

<sup>1</sup>Institute of Chemistry, ELTE Eötvös Loránd University, Budapest, Hungary. <sup>2</sup>Department of Chemistry, University of Vermont, Burlington, VT, USA. <sup>3</sup>Department of Theoretical Physics, University of Debrecen, Debrecen, Hungary. <sup>4</sup>ELTE Hevesy György PhD School of Chemistry, Budapest, Hungary. <sup>5</sup>Department of Chemistry and Biochemistry, Auburn University, Auburn, AL, USA. e-mail: [roland.tobias@ttk.elte.hu](mailto:roland.tobias@ttk.elte.hu); [attila.csaszar@ttk.elte.hu](mailto:attila.csaszar@ttk.elte.hu)

contaminant species, and (b) computational artifacts, arising from the use of inaccurate potential energy (PES) and property surfaces (often in combination with deficiencies of the dynamical models applied).

The first step toward the accurate first-principles computation of CIA spectra is the determination of an accurate potential energy surface (PES). About this a lot of experience has been gained over the past few decades, especially for binary van der Waals complexes; see, for example, refs. 32–44. To build reliable analytical PESs for NCI complexes like  $\text{N}_2\text{-N}_2$ , highly flexible model functions must be selected, trained on NCI energies at a large number of grid points. For the accurate computation of these rather small NCI energies, not only electron-correlation effects have to be taken into account, but the basis-set incompleteness and superposition errors should also be minimized. All this has usually been achieved *via* the “gold standard” CCSD(T) (that is, the coupled cluster singles, doubles, and iterative triples) method<sup>45</sup>, combined with extrapolation<sup>46,47</sup> and counterpoise-correction<sup>48</sup> schemes. To increase accuracy, consideration of so-called “small corrections”<sup>49,50</sup> may also become necessary. Convergence of the individual correlation-energy increments to relative energies can be traced with the help of the focal-point analysis (FPA) scheme<sup>49,51</sup>, yielding the ultimate first-principles estimates, with definitive uncertainties<sup>52</sup>, for the NCI energies at particular configurations or over the entire PES<sup>53</sup>. If coupled-cluster computations are unaffordable for a complex, symmetry-adapted perturbation theory (SAPT) protocols<sup>54–58</sup> provide excellent alternatives.

Over the past few decades, several first-principles and empirical PESs have been developed for the  $\text{N}_2$  dimer<sup>59–73</sup>, though most of them within the rigid-monomer approximation (*i.e.*, keeping the two  $\text{N}\equiv\text{N}$  bond lengths fixed, resulting in four-dimensional (4D) dynamical models). Exceptions are the two full-dimensional (6D) PESs of the Truhlar group<sup>74,75</sup>, designed for the investigation of high-energy rovibrational energy transfer and collision-induced monomer dissociation in the  $\text{N}_2\text{-N}_2$  system. These PESs, unfortunately, have only chemical ( $\sim 350 \text{ cm}^{-1}$ ) accuracy. Among the 4D surfaces, Hellmann’s scaled benchmark PES<sup>72</sup> has the highest accuracy, approaching the full configuration interaction (FCI) and complete basis set (CBS) limits<sup>33,53</sup> and involving small corrections<sup>49</sup> at vibrationally averaged monomer bond lengths. This 4D PES leaves no doubt that the global minimum of the  $\text{N}_2$  dimer is a planar tilted structure of  $C_{2h}$  point-group symmetry, in contrast to PESs exhibiting T-shaped<sup>62,66,71</sup> or nonplanar “twisted”<sup>59,60,63</sup> global minima. Such discrepancies can be ascribed to the lack of accurate first-principles data points and the use of over-simplified functional forms<sup>76</sup>.

Despite the extensive literature available on other binary complexes, see, *e.g.*, refs. 32,37,38,40,41,43,44, to the best of our knowledge, there are only three articles<sup>66,77,78</sup> reporting bound-state rovibrational computations on  $\text{N}_2\text{-N}_2$ . In a first, ground-breaking study, Tennyson and van der Avoird<sup>77</sup> employed a rigid-monomer Hamiltonian and a simple 4D PES<sup>59</sup>, with a twisted global minimum of  $D_{2d}$  point-group symmetry (this PES was fitted to SAPT-like computations involving Hartree–Fock monomer wavefunctions and small Gaussian basis sets). This analysis produced a large number of bound states for  $J \leq 2$  (specifically, 92 for  $J = 0$ ), where  $J$  denotes the overall rotational quantum number. Next, Brocks and van der Avoird<sup>78</sup> simulated the far- and mid-infrared spectra of  $^{14}\text{N}_2\text{-}^{14}\text{N}_2$ , using the formalism of ref. 77, up to  $J = 7$ . A similar protocol was followed by Aquilanti et al., but with a fully empirical PES parametrized for scattering experiments, whose global minimum has a T-shaped form<sup>66</sup>. They computed bound rovibrational states up to  $J = 6$ . Unfortunately, all of these otherwise sophisticated studies relied on qualitatively incorrect PESs, as the global minimum is neither twisted nor T-shaped<sup>72,76</sup>.

In this work, the structure, the rovibrational energy levels, and the nuclear dynamics of  $\text{N}_2\text{-N}_2$  are reconsidered, using exact kinetic-energy operators and highly accurate PESs. The potentials used include Hellmann’s 4D PES<sup>72</sup> and two newly created 6D PESs, with the more accurate one having spectroscopic ( $1 \text{ cm}^{-1}$ ) accuracy. The present investigation delivers an exhaustive list of bound rovibrational states for the  $^{14}\text{N}_2\text{-}^{14}\text{N}_2$  dimer up to  $J = 10$ , with state-by-state uncertainty estimates and correct symmetry labels corresponding to the irreducible representations of the  $G_{16}$  molecular symmetry group<sup>79</sup>. For the first time, accurate shifts and splittings are

deduced for the intramonomer stretch fundamentals, representing quasi-bound (resonance) states. For the lowest doubly degenerate vibrational state of  $^{14}\text{N}_2\text{-}^{14}\text{N}_2$ , isotope effects are also considered. Based on our extensive computational results, it can be firmly established that  $\text{N}_2\text{-N}_2$  behaves as a quasistructural<sup>80</sup> complex, whose highly unusual and interesting rovibrational states fail interpretation attempts based on the simplest rigid rotor and harmonic oscillator models.

## Results and discussion

Perhaps the most significant finding of this article is that it provides clear evidence for the quasistructural nature<sup>80</sup> of the nitrogen dimer, a prototype of weakly-bound vdW dimers. This conclusion is based on cutting-edge electronic-structure and quasi-)variational nuclear-motion computations<sup>81</sup>, employing exact kinetic-energy operators both in reduced and full dimensions. Following some introductory remarks, our discussion focuses only on the analysis of the numerical results, while the important technical details about the computational methodology employed are contained in Section “Methods” and in Supplementary Notes 1–4. Apart from Section “Isotope effects”, our rovibrational and dynamical results concern the parent  $\text{N}_2\text{-N}_2$  isotopologue,  $^{14}\text{N}_2\text{-}^{14}\text{N}_2$ .

First, results of rigorous tests performed to determine the level of electronic-structure theory needed to obtain a highly accurate, spectroscopically meaningful, full-dimensional PES for  $\text{N}_2\text{-N}_2$  are discussed (see Fig. 1). Second, five salient stationary points on the PES of  $\text{N}_2\text{-N}_2$ , Z, T, X, H, and I (see Fig. 2), are investigated. Third, results from our benchmark-quality first-principles rovibrational computations, yielding a large number of bound and a few resonance (quasi-bound)<sup>82</sup> states are summarized. Fourth, the peculiar characteristics of these (ro)vibrational quantum states are explored *via* probability-density analyses, offering an interpretation of the computational results.

## Potential energy surfaces and stationary points

To decide about the level of electronic-structure theory that should be used to develop an analytical PES for  $\text{N}_2\text{-N}_2$  with spectroscopic ( $\approx 1 \text{ cm}^{-1}$ ) accuracy, the computational results of Hellmann<sup>72</sup>, called here H0B and produced at a high, composite level of electronic-structure theory, have been taken as reference values. Since our aim has been to supervise the construction of the PES with the autoPES program system<sup>35,39</sup>, used successfully by us during a similar project<sup>83</sup>, the present analysis focuses on levels of electronic-structure theory directly supported by this package through its interfaces. Specifically, two levels are considered, referred to as “SAPT” and “CC” (always with double quotes) throughout this paper (for technical details about the H0B, “SAPT”, and “CC” levels, see Section “Electronic-structure computations”).

Figure 1 illustrates the unsigned deviations of our intermonomer energies from their H0B counterparts at grid points selected, up to 10,000  $\text{cm}^{-1}$ , from the list of Hellmann<sup>72</sup>. In Fig. 1(a), a remarkably good agreement is seen between the results of the coupled-cluster-based “CC” and the H0B protocols, translating to sub- $\text{cm}^{-1}$  agreement for the majority of the structures with dominant vdW attractions. As apparent from Fig. 1(b), the “SAPT” energies also agree well with Hellmann’s benchmark values, though the differences are mostly larger here than in the “CC” case. This encouraged us to create two 6D surfaces, named N2d-CC and N2d-SAPT, fitted to “CC” and “SAPT” energies, respectively, whose parametrization did not benefit from Hellmann’s grid points. The two PESs nicely reproduce the H0B energies, to the same extent as the direct “CC”/“SAPT” computations [see Fig. 1(c)/(d)]. These two PESs (see Section “PES construction” how they were created), along with Hellmann’s original (H0B-based) PES designated here as N2d-H0B, have been applied in our rovibrational and dynamical analyses.

To explore the stationary points (SP) of the N2d-H0B, N2d-CC, and N2d-SAPT PESs, extensive global searches have been made, revealing altogether five salient SPs with relatively high point-group symmetries (see Fig. 2). These five nuclear arrangements could be identified as SPs on all three PESs and their orders are consistent across the different PESs. To name

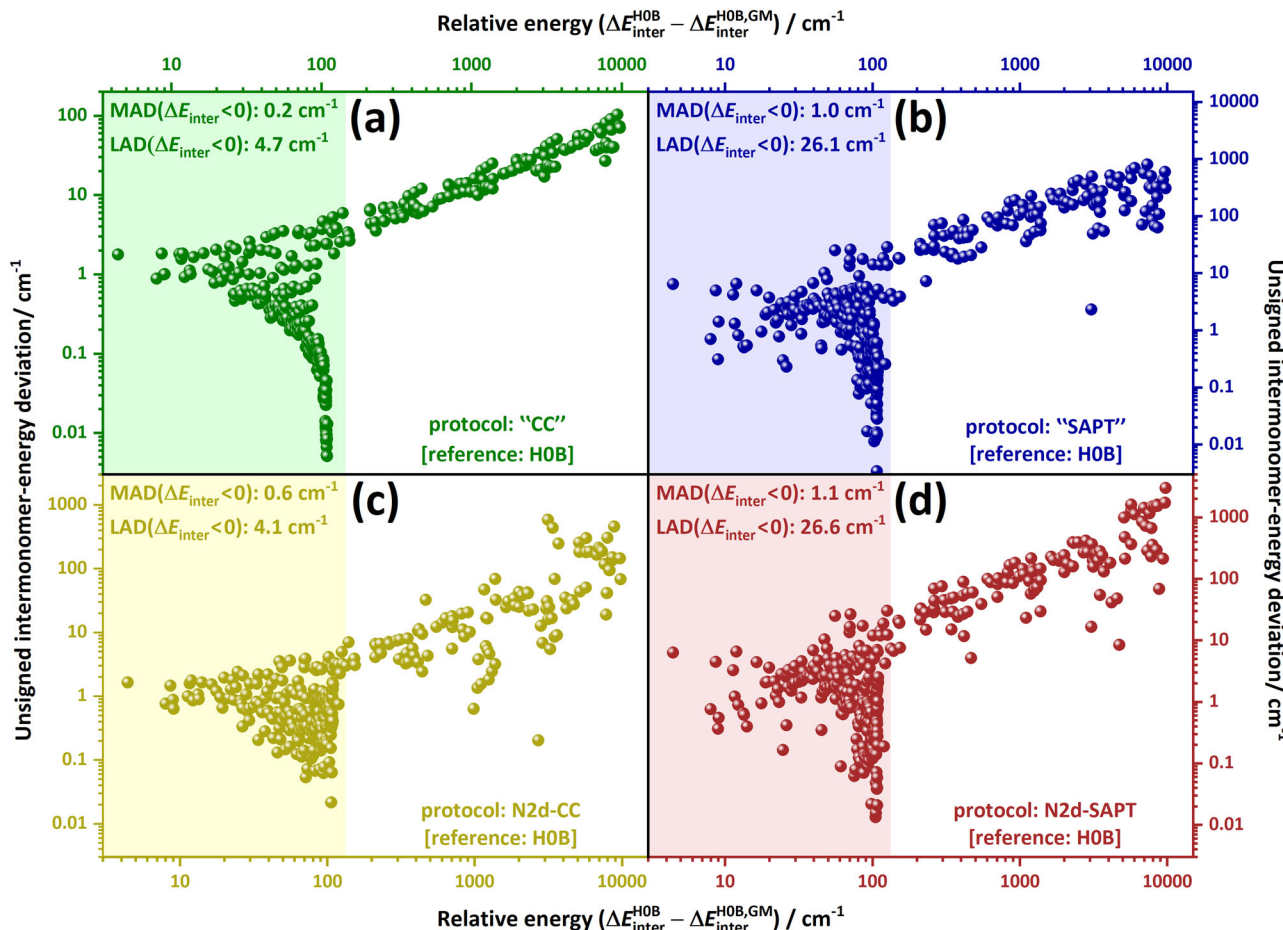


**Fig. 1 | Comparison of the intermonomer energies of the N<sub>2</sub> dimer using various levels of electronic structure theory.** The panels depict the deviations of the direct electronic-structure results (a, b) and their fitted counterparts (c, d) from the HOB reference values. For the “C”, “SAPT”, N2d-CC, N2d-SAPT, and HOB protocols, see Section “Methods”. The reference grid points and their benchmark (HOB) intermonomer energies are taken from ref. 72, whereas the other (non-HOB) data were obtained during the present study. The relative energies are taken with respect to the

intermonomer energy at the global minimum of the HOB energy scheme, with  $\Delta E_{\text{inter}}^{\text{HOB,GM}} \approx -109.21 \text{ cm}^{-1}$ <sup>72</sup>. The colored boxes on the left-hand side of each panel highlight points whose intermonomer energies are below the dimer’s approximate dissociation limit,  $-\Delta E_{\text{inter}}^{\text{HOB,GM}}$ . In these boxes, the median absolute deviations (MAD) and the largest absolute deviations (LAD) pertaining to dimer geometries with negative intermonomer energies are also given.

these SPs, the convention applied in ref. 74 has been adopted (see Fig. 2). Our results show that (a) the tilted, Z-shaped form is the only minimum on these three PESs, and (b) the intramonomer effects are minuscule, at most 0.05 cm<sup>-1</sup> for the relative interaction energies, for the five SPs considered (see Fig. 2 and Supplementary Table 2 for the structural and interaction parameters of these SPs).

As a next step, detailed FPA analyses<sup>49,51</sup> were performed for three of the five SPs to further validate the accuracy of the N2d-CC/SAPT PESs (see Supplementary Note 1). The resulting interaction energies, alongside their estimated uncertainties in parentheses, are collected in Supplementary Table 2 (note that part of the electronic-structure results concerning the global minimum was taken from ref. 36). The various interaction-energy determinations agree nicely: in fact, almost all of the deviations fall within or are at least reasonably close to the ultimate FPA uncertainties. As to the correlation-energy increments given in Supplementary Table 1 for the three SPs studied *via* FPA, each post-CCSD(T) term is below  $\pm 6 \text{ cm}^{-1}$ , and they have rather similar values, mostly with the same signs. Thus, these contributions cancel each other to a large extent in the relative interaction energies, a typical effect for non-covalent complexes<sup>84</sup>.

### First-principles rovibrational results

Making use of the three PESs discussed in Sec. 2.1, variational nuclear-motion computations, always with exact kinetic-energy operators, have

been carried out, exploiting the permutation-inversion symmetry of the dimer (see Section “Symmetry-adapted variational nuclear-motion computations”). This subsection gives a description of the computational results obtained, including accurate rovibrational energies of the <sup>14</sup>N<sub>2</sub>·<sup>14</sup>N<sub>2</sub> complex both below and above the first dissociation limit, corresponding to bound and resonance states, respectively. The results reported take advantage of four dynamical models of different dimensionality, that is 6D, 4D, 4D0, and 2D, introduced for the N<sub>2</sub> dimer in Section “Internal coordinates and nuclear-motion models”. The discussion itself is divided into four parts, focusing on the zero-point vibrational effect, the bound and then the resonance states, and on isotope effects.

**Zero-point vibrational effects.** Employing the FPA protocol<sup>49,51</sup>, the electronic interaction energy,  $\Delta E_{\text{int}}$ , is estimated to be  $-109.3 \pm 2.6 \text{ cm}^{-1}$  for the global minimum of N<sub>2</sub>·N<sub>2</sub>. Compared to this value, the zero-point vibrational energy (ZPVE) correction,  $\delta E_{\text{int}}^{\text{ZPVE}}$ , is substantial (see Table 1); thus, knowing its value accurately is essential to characterize the thermodynamic stability of the N<sub>2</sub> dimer at absolute zero temperature. In particular, the sum of these two terms is the interaction (Gibbs) free energy at 0 K,  $\Delta G_{\text{int}}^0$ , whose absolute value equals the first dissociation limit of (N<sub>2</sub>)<sub>2</sub> (this quantity is also needed to find the highest-energy bound state in the dimer’s energy spectrum for each  $J$  value).

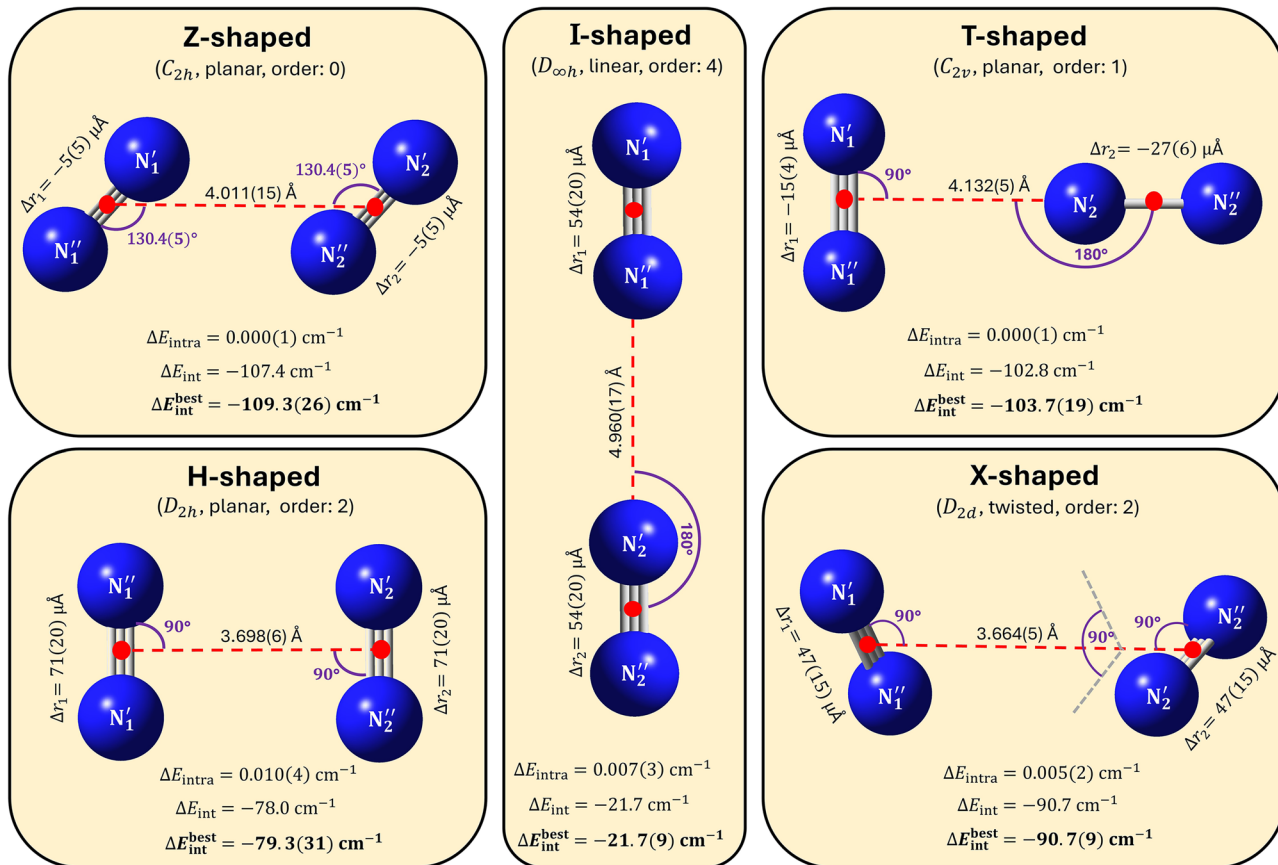


**Fig. 2 | Five salient stationary points on three analytical potential energy surfaces (PES) of  $\text{N}_2\text{-N}_2$ .** For parameter values affected by computational error, the last-digit (two-sigma) uncertainties are given in parentheses. The boldfaced  $\Delta E_{\text{int}}^{\text{best}}$  values represent the best estimates of this study. All the other parameter values correspond to the N2d-CC PES [see also Section “Potential energy surfaces and stationary points” and Supplementary Note 1]. The stationary-point order, *i.e.*, the number of negative Hessian eigenvalues, is given for each shape next to its point-group symmetry. As customary, the intermonomer coordinates (see Section “Internal

coordinates and nuclear-motion models”) are indicated with (dashed) lines and arcs. Instead of the  $r_1$  and  $r_2$  bond lengths, the  $\Delta r_1$  and  $\Delta r_2$  relative values are displayed, respectively (these relative distances are referenced to the equilibrium bond length of the isolated  $\text{N}_2$  unit; see Section “Internal coordinates and nuclear-motion models”). The intramonomer energies,  $\Delta E_{\text{intra}}$ , are negligibly small for all five geometries (see Section “PES construction”). The uncertainty estimates are based on the deviations between the N2d-SAPT/H0B and N2d-CC results.

**Table 1 | Electronic and zero-point vibrational effects in the Z-shaped global minimum of the  $\text{N}_2$  dimer<sup>(a)</sup>**

Potential <sup>(b)</sup>	$\Delta E_{\text{int}}^{\text{(c)}}$	$\delta E_{\text{int}}^{\text{ZPVE}}^{\text{(d)}}$	$\Delta G_{\text{int}}^0$ <sup>(e)</sup>			ZPVE( $\text{N}_2 \cdot \text{N}_2$ ) <sup>(f)</sup>		
			4D	4D0	6D	4D	4D0	6D
N2d-H0B	-109.2	35.5				-73.7		
N2d-CC	-107.4	35.4	35.2	35.2	-72.0	-72.2	-72.2	2387.0
N2d-SAPT	-106.3	33.9	33.6	33.6	-72.4	-72.7	-72.7	2385.4
Best <sup>(g)</sup>	<b>-109.3(26)</b>	<b>35.2(3)</b>				<b>-72.2(15)</b>		<b>2386.7(16)</b>

<sup>(a)</sup>All numerical values are given in  $\text{cm}^{-1}$ .

<sup>(b)</sup>The analytical potential energy surfaces are defined in Section “Potential energy surfaces and stationary points”.

<sup>(c)</sup>Estimates for the interaction energy of the Z-shaped global minimum from Supplementary Table 2.

<sup>(d)</sup>First-principles zero-point vibrational energy (ZPVE) corrections determined with different potentials and dynamical models (see also Section “Internal coordinates and nuclear-motion models”).  $\delta E_{\text{int}}^{\text{ZPVE}}$  refers to the change due to the intermolecular vibrational modes.

<sup>(e)</sup>Variational estimates for the zero-point-corrected interaction energy (*i.e.*, the interaction free energy at 0 K).

<sup>(f)</sup>Variational ZPVE values for the Z-shaped global minimum. 2D + 4D means the sum of the ZPVEs corresponding to the 2D and 4D dynamical models.

<sup>(g)</sup>Best predictions obtained for the four quantities are highlighted in boldface and their expanded (two-sigma) uncertainties are in parentheses.

Table 1 lists various predictions for three quantities,  $\Delta E_{\text{int}}$ ,  $\delta E_{\text{int}}^{\text{ZPVE}}$ , and  $\Delta G_{\text{int}}^0$ , extracted from our electronic structure and variational nuclear-motion computations. Apparently, the variational  $\delta E_{\text{int}}^{\text{ZPVE}}$  and  $\Delta G_{\text{int}}^0$  values barely change across the different dynamical models and PESs: their maximum unsigned deviations are as low as 1.1 and 1.5  $\text{cm}^{-1}$ , respectively (based on the deviations observed, uncertainty estimates have been adopted for the

best predictions of all these quantities). A harmonic force field, computed at the frozen-core CCSD(T) level using an augmented quadruple-zeta basis set<sup>85</sup>, provides  $\delta E_{\text{int}}^{\text{ZPVE}} = 49.2 \text{ cm}^{-1}$ , which differs significantly, by as much as 14  $\text{cm}^{-1}$ , from our accurate variational estimate, 35.2(3)  $\text{cm}^{-1}$ . Interestingly, previous  $\Delta G_{\text{int}}^0$  predictions,  $-79.8^{66}$  and  $-75.0^{78} \text{ cm}^{-1}$ , are reasonably close to our best estimate,  $-72.2(15) \text{ cm}^{-1}$ , although they are based, respectively,

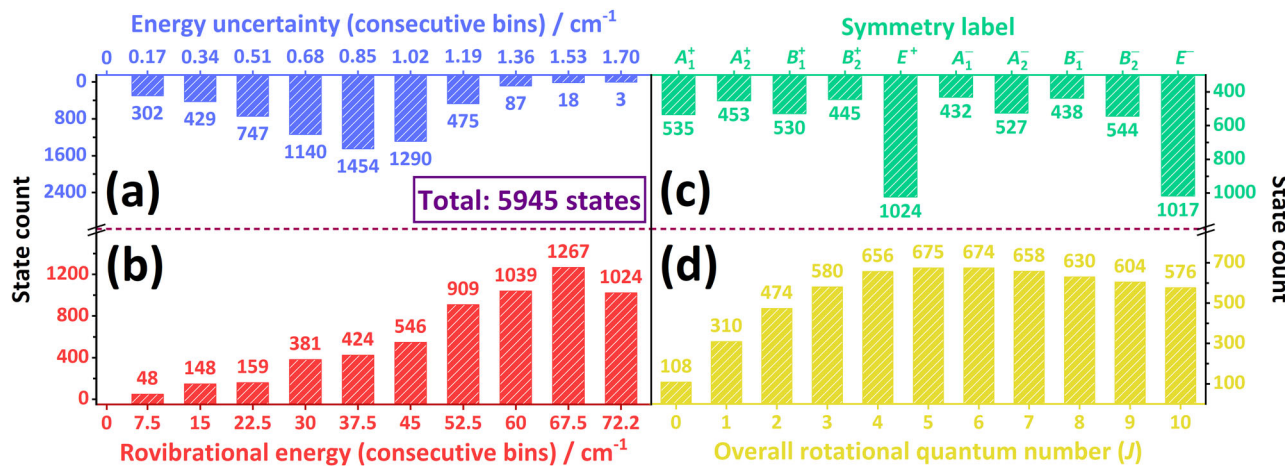


**Fig. 3 | Statistical characteristics of the bound rovibrational states obtained during this study.** In (a, b), the range represented by a bin is given by the actual and the previous axis ticks (e.g., the blue bin at  $0.17\text{ cm}^{-1}$  contains states with an

uncertainty of  $0.00\text{--}0.17\text{ cm}^{-1}$ ). In contrast, the horizontal axes of (c, d) have discrete (integer) values. The state counts, *i.e.*, the bin sizes, are shown on a unified bi-directed vertical axis for both pairs of distributions.

on PESs with (incorrect) T- and X-shaped global minima (the small deviations observed are most likely due to the extremely similar interaction energies characterizing these qualitatively different structures).

**Bound states.** Accurate rovibrational energies have been computed for nearly 6000 bound states of  $^{14}\text{N}_2\text{--}^{14}\text{N}_2$ , taking advantage of our improved methodology described in Section “Symmetry-adapted variational nuclear-motion computations”. The list of the computed energy levels, including all rovibrational states with  $J \leq 10$  below the first dissociation limit, is given in an external repository<sup>86</sup> through an Excel file. Readers interested in individual characteristics of these bound states, such as the “raw” energy values produced *via* various dynamical models and PESs, are invited to study that file. In what follows, our discussion is focusing on some overall statistical measures, illustrated in Fig. 3.

On the left two panels of Fig. 3 the state distributions represent two continuous measures, namely the rovibrational energies [panel (b)] and their uncertainties [panel (a)]. As expected, the overwhelming majority of the bound states, more than 80 % of them, fall above half of the dissociation energy. Nevertheless, there are also dozens of states in the lowest energy bin,  $0\text{--}7.5\text{ cm}^{-1}$ , reflecting the weakly-bound nature and the relative heaviness of  $\text{N}_2\text{--N}_2$ . Most of the uncertainty, defined in Eqs. (4) and (5) and stretching over the  $0\text{--}1.7\text{ cm}^{-1}$  range, comes from intermonomer effects, while the error contributions due to intramonomer motions remain below  $0.15\text{ cm}^{-1}$ .

The two right-hand-side panels of Fig. 3 are based on two discrete variables, namely the  $J$  values [panel (d)] and the symmetry blocks [*i.e.*, irreducible representations (irreps) of the  $G_{16}$  group, panel (c)]. The distribution along the  $J$  values has a maximum at  $J = 5$ : from that point on, the  $(2J + 1)$ -fold rotational degeneracy ceases to be the dominant factor over the energy cutoff represented by the dissociation energy. It is of interest to observe in Fig. 3(c) that the blocks  $E^+$  and  $E^-$ , even though their two-fold degenerate states are counted only once, are about twice as large as the other blocks. The small energy of the lowest  $E^+$  state may explain this (see also Section “Isotope effects”), as it can form several combination bands with other one-dimensional irreps.

**Resonance states.** Among the large number of resonance states<sup>82</sup> one may compute for  $^{14}\text{N}_2\text{--}^{14}\text{N}_2$ , attention is focused here only on the two long-lived intramonomer stretch fundamentals. The symmetric (sSTRE) and the antisymmetric (aSTRE) stretch states transform according to the  $A_1^+$  and  $B_2^+$  irreps of the  $G_{16}$  molecular symmetry group, respectively.

Since the sSTRE and aSTRE states lie at least 30 times higher than the dissociation limit, their computation was greatly accelerated by the exploitation of the block-diagonal structure of the Hamiltonian; in particular, our computations were restricted to the  $A_1^+$  and  $B_2^+$  blocks in this energy domain, a considerable gain in efficiency. The relatively small basis set sufficient to achieve converged sSTRE/aSTRE energies also helped (see Section “Methods”).

Table 2 includes multiple determinations for the shifts and splittings of the sSTRE and aSTRE fundamentals, all relative to the energy of the fundamental of the  $\text{N}_2$  monomer. The best results, corresponding to the full-dimensional  $\text{N}2\text{d-CC}$  PES, are given in the last row of Table 2 (typeset in boldface). Clearly, there are pronounced changes in these shifts/splittings across the different PESs and their intermediate versions; thus, estimating the uncertainties of these computed quantities is exceedingly difficult (the value of  $\pm 0.1\text{ cm}^{-1}$ , stated in Table 2, is a conservative estimate). As the even larger errors of the 2D predictions suggest, the intra- and intermonomer couplings result in non-negligible contributions to these quantities.

Although the final computed shifts and splittings are small, below  $1\text{ cm}^{-1}$ , they are significant given the accuracy and resolution of today’s spectroscopic measurements. Accordingly, it seems feasible to generate experimental information about the energy ordering of the free stretch of  $\text{N}_2$  and the sSTRE and aSTRE fundamentals of  $^{14}\text{N}_2\text{--}^{14}\text{N}_2$ , however small the differences are.

**Isotope effects.** Table 3 shows the effects of isotopic substitution for the lowest two excited vibrational states of the six possible  $^{14}\text{N}$  and  $^{15}\text{N}$  isotopologues, with symmetry labels provided for each case. The double degeneracy, characterizing these two vibrational modes in the  $^{14}\text{N}_2\text{--}^{14}\text{N}_2$  dimer, is lifted for the mixed isotopologues, where both  $^{14}\text{N}$  and  $^{15}\text{N}$  are present, inducing small shifts and splittings. The largest shift is, of course, for the fully symmetric  $^{15}\text{N}_2\text{--}^{15}\text{N}_2$  isotopologue, for which there is again no splitting. These quantities turned out to be insensitive to the details of the PES used for their computation, leading to estimated uncertainties on the order of  $10^{-3}\text{ cm}^{-1}$  (see Table 3).

As expected, the shifts of Table 3 are always negative, and their absolute values increase with the number of  $^{15}\text{N}$  atoms in the dimer. Assuming  $\Delta\mathcal{M}_1 \leq \Delta\mathcal{M}_2$ , where  $\Delta\mathcal{M}_i$  is the change in the mass of the  $i$ th monomer compared to that of the  $^{14}\text{N}_2$  isotopologue, the shifts of the vibrational modes  $\text{vib}_1$  and  $\text{vib}_2$  closely follow a simple model,

$$\text{shift}(\text{vib}_i) \approx a_1 \Delta\mathcal{M}_i + a_2 \Delta\mathcal{M}_{3-i}, \quad (1)$$

**Table 2 | Computed shifts and splittings in the two intramonomer stretch fundamentals of  $^{14}\text{N}_2\cdot^{14}\text{N}_2$ <sup>(a)</sup>**

Estimate <sup>(e)</sup>	Shift(sSTRE) <sup>(b)</sup> [ $A_1^+$ ]		Shift(aSTRE) <sup>(c)</sup> [ $B_2^+$ ]		Splitting <sup>(d)</sup>	
	2D	6D	2D	6D	2D	6D
Range(N2d-SAPT)	[0.10, 0.32]	[-0.36, -0.18]	[-0.29, -0.06]	[-0.43, -0.30]	[-0.41, -0.27]	[-0.12, -0.05]
Best(N2d-SAPT)	0.13	-0.33	-0.17	-0.38	-0.30	-0.05
Range(N2d-CC)	[0.10, 0.31]	[-0.21, -0.15]	[-0.25, -0.09]	[-0.35, -0.28]	[-0.40, -0.34]	[-0.17, -0.10]
Best(N2d-CC)	0.26	<b>-0.19(10)</b>	-0.09	<b>-0.28(10)</b>	-0.35	<b>-0.10(10)</b>

<sup>(a)</sup>All numerical data are in  $\text{cm}^{-1}$ . The full-dimensional ‘best’ cases are attached with expanded (two-sigma) uncertainty estimates.

<sup>(b,c)</sup>Shift of the symmetric/antisymmetric stretch (sSTRE/aSTRE) fundamental, relative to its counterpart in the free  $\text{N}_2$  molecule, 2329.912  $\text{cm}^{-1}$ <sup>11</sup>. The symmetry labels of the sSTRE/aSTRE states, within the  $G_{16}$  molecular symmetry group, are given in brackets. For the 2D/6D model, see Section “Internal coordinates and nuclear-motion models”.

<sup>(d)</sup>Energy difference defined as aSTRE – sSTRE.

<sup>(e)</sup>Estimates using the N2d-CC and N2d-SAPT potential energy surfaces (PES). The best values, typeset in boldface, are derived via the final versions of the two PESs, while the ranges are deduced from five intermediate PES versions produced during the PES-refinement process.

**Table 3 | Isotope effects in the first two excited vibrational states of the  $\text{N}_2$  dimer<sup>(a)</sup>**

Species <sup>(b)</sup>	Group <sup>(c)</sup>	vib <sub>1</sub> <sup>(d)</sup>			vib <sub>2</sub> <sup>(e)</sup>			Splitting <sup>(f)</sup>
		Label <sup>(f)</sup>	Shift <sup>(g)</sup>	Dev. <sup>(h)</sup>	Label <sup>(f)</sup>	Shift <sup>(g)</sup>	Dev. <sup>(h)</sup>	
$^{14}\text{N}_2\cdot^{14}\text{N}_2$	$G_{16}$	$E^+$	0.0	0.0	$E^+$	0.0	0.0	0.0
$^{14}\text{N}_2\cdot^{14}\text{N}^{15}\text{N}$	$G_4$	$A^+$	-0.111(1)	0.001	$B^+$	-0.060(2)	0.001	0.051(1)
$^{14}\text{N}_2\cdot^{15}\text{N}_2$	$G_8$	$B''_2$	-0.226(3)	-0.001	$B'_2$	-0.123(1)	-0.001	0.103(4)
$^{14}\text{N}^{15}\text{N}\cdot^{14}\text{N}^{15}\text{N}$	$G_4$	$B^+$	-0.171(2)	0.002	$A^+$	-0.170(3)	0.003	0.001(1)
$^{14}\text{N}^{15}\text{N}\cdot^{15}\text{N}_2$	$G_4$	$B^+$	-0.285(1)	0.001	$A^+$	-0.233(2)	0.001	0.052(3)
$^{15}\text{N}_2\cdot^{15}\text{N}_2$	$G_{16}$	$E^+$	-0.346(2)	0.001	$E^+$	-0.346(2)	0.001	0.0

<sup>(a)</sup>All numerical data are given in  $\text{cm}^{-1}$ , with the (two-sigma) uncertainties of their last few digits in parentheses. For the calculation of these uncertainties, Eq. (4) was applied, but replacing the absolute energies with shifts/splittings.

<sup>(b)</sup>Isotopologue of the  $\text{N}_2\cdot\text{N}_2$  complex, composed of  $^{14}\text{N}$  and/or  $^{15}\text{N}$  isotopes with spin-1 and spin-1/2 nuclei, respectively.

<sup>(c)</sup>Molecular symmetry group of a particular species.

<sup>(d,e)</sup>First/second excited vibrational state of a given isotopologue.

<sup>(f)</sup>Symmetry label associated with a specific state of this table.

<sup>(g)</sup>Shifts of the first two excited vibrational energies with respect to their degenerate sibling in the  $^{14}\text{N}_2\cdot^{14}\text{N}_2$  species, 3.57(3)  $\text{cm}^{-1}$ .

<sup>(h)</sup>Deviation of a shift predicted via Eq. (1) from its variational counterpart. The monomer masses behind Eq. (1) rely on  $^{14}\text{N}$  and  $^{15}\text{N}$  masses defined in Section “Methods”.

<sup>(i)</sup>Energy splitting between vib<sub>1</sub> and vib<sub>2</sub>, which is equivalent to shift(vib<sub>1</sub>) – shift(vib<sub>2</sub>).

where  $a_1 = -0.060\ 8(9)\ \text{cm}^{-1}\ \text{u}^{-1}$  and  $a_2 = -0.112\ 5(9)\ \text{cm}^{-1}\ \text{u}^{-1}$  are two fitted parameters, which perfectly coincide with the two shifts of the  $^{14}\text{N}_2\cdot^{14}\text{N}^{15}\text{N}$  complex [see Supplementary Note 4 for the derivation of Eq. (1)]. These shifts and splittings are straightforwardly measurable; thus, their accurate estimates given in Table 3 should become useful guides during the interpretation of the related spectroscopic experiments.

### Manifestation of quasistructurality of the $\text{N}_2\cdot\text{N}_2$ complex

In ref. 80, it was proposed that a molecular system should be called quasistructural if it satisfies all of the following five criteria: (i) “the notion of a static equilibrium structure, corresponding to a minimum on the potential energy surface of the molecule, loses its strict meaning”, (ii) “internal nuclear motions [...] become dominant, resulting in an effective molecular structure often even qualitatively different from the equilibrium one”, (iii) “separation of the internal nuclear motions breaks down, rotational and vibrational degrees of freedom cannot be separated from each other when interpreting even the lowest rovibrational eigenstates of the molecule, often resulting in effective rotational constants drastically different from the equilibrium ones even for the ground vibrational eigenstate”, (iv) “classification of the rovibrational states requires the use of permutation-inversion symmetry”, and (v) “some of the rovibrational eigenenergies assigned to a vibrational parent state exhibit unconventional [...] rotational contributions”. In the upcoming analysis, our aim is to study how closely these criteria are met for  $\text{N}_2\cdot\text{N}_2$ .

It is important to clarify the relation of quasistructural molecules<sup>80</sup> to floppy and fluxional/fluxional<sup>87</sup> systems. In floppy molecules, there are one or more large-amplitude internal motions, but their rotational energy-level structure may be fitted well by a rigid or a semirigid effective Hamiltonian.

As noted by Bunker and Jensen<sup>79</sup> about ethane, “except in ultrahigh resolution spectroscopic studies ethane can be considered to be a rigid molecule.” Fluxional systems exhibit rapid, degenerate rearrangements among physically equivalent structures. Although quasistructural molecules necessarily fall under the broader categories of floppy or fluxional systems, the converse is not true. Quasistructurality denotes a more specific structural and dynamical behavior, one accompanied by a qualitative breakdown of standard spectroscopic paradigms. In particular, the commonly assumed separation of rotational and vibrational motion is already not valid even for the lowest-energy states (see below).

**Extremely flat interaction PES.** According to the interaction energies given in Fig. 2, the Z-shaped global minimum of the  $\text{N}_2$  dimer lies below the T-shaped transition state by only roughly 6  $\text{cm}^{-1}$ . Moreover, two other salient, higher-order saddle points, X and H, are also energetically similar to the Z-shaped minimum. This suggests that the PES is shallow over a large part of the interacting regime. To gain deeper insight into the overall topology of the PES in the most important regions, contour plots have been constructed for the  $(r_1, r_2)$ ,  $(R, \phi)$ , and  $(\theta_1, \theta_2)$  coordinate pairs (see the three panels of Fig. 4).

As expected and apparent from Fig. 4(a), the energy increases sharply when the  $r_1$  and  $r_2$  coordinates describing the two monomer stretches are distorted. To help interpret Fig. 4(a), recall the minuscule  $\Delta r_1$  and  $\Delta r_2$  values of Fig. 2 and the small shifts and splittings displayed in Table 2. As seen in Fig. 4(b), the  $R$  variable, that is the dimer’s vdW dissociation coordinate, is relatively tightly bound at its equilibrium value,  $\sim 4.0\ \text{\AA}$ . In clear contrast, motion along the torsional coordinate  $\phi$  is extremely soft, without

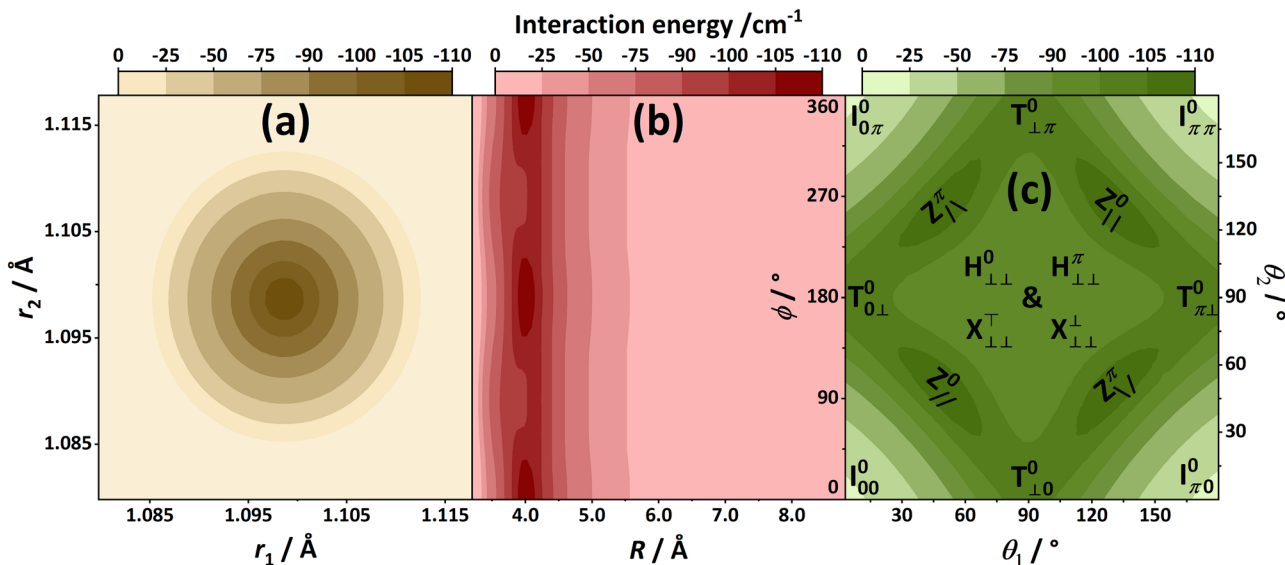


**Fig. 4 |** Contour plots determined from two-dimensional (2D) scans of the N<sub>2</sub>·CC potential energy surface (PES). For each 2D point, the remaining four variables were fully relaxed. The contour levels represent interaction energies, with scales given separately on the top of each panel. The energetically equivalent Z-, T-, H-, X-,

and I-shaped forms are shown explicitly in panel (c), following the  $S_{\theta_1 \theta_2}^{\phi}$  notation for a shape  $S$ , where the specific angle values are  $\approx 49.5^\circ$ ,  $\perp \equiv 90^\circ$ ,  $\backslash \approx 130.5^\circ$ ,  $\pi \equiv 180^\circ$ , and  $T \equiv 270^\circ$ .

considerable barriers over the complete  $[0, 2\pi]$  angular range, as shown in Fig. 4(b). As obvious from Fig. 4(c), the Z-shaped form can also distort quite easily along the two bending coordinates, there is no pronounced angular preference in the broad, dark-green domain. These observations leave no doubt that the N<sub>2</sub> dimer complies with criterion (i) of quasistructurality.

**Heavily mixed vibrational states.** To gain insight into the vibrational characteristics of N<sub>2</sub>·N<sub>2</sub>, probability densities have been generated for all the bound  $J = 0$  states of <sup>14</sup>N<sub>2</sub>·<sup>14</sup>N<sub>2</sub>, as well as for its two intramonomer stretch fundamentals. Density distributions of the first four vibrational states, of  $A_1^+$ ,  $E^+$ ,  $B_1^+$ , and  $A_1^-$  symmetry, in order, are shown in Fig. 5 (plots of the other  $J = 0$  states are available in an external repository<sup>86</sup>). Since the  $(r_1, r_2)$  graphs exhibit a simple and regular ground-state density profile for the bound states, without noticeable variations, in Fig. 5 density distributions are given solely for the  $(R, \phi)$  and  $(\theta_1, \theta_2)$  subspaces. Supplementary Fig. 1 provides a density-based comparison between the ground state and the two intramonomer fundamentals, where the  $(r_1, r_2)$  plots are also included.

In accordance with the flatness of the interaction PES along the three angular coordinates (see Section “Extremely flat interaction PES”), the density distributions of Fig. 5 show that the nuclei of N<sub>2</sub>·N<sub>2</sub> are prone to delocalization along all three of them. This is true even for the ground vibrational state, where (a) along the torsional coordinate  $\phi$ , at fixed  $R$  values the density does not vary noticeably [see Fig. 5(a)], and (b) the points with high densities are accumulated in the broad and square-shaped central part of Fig. 5(d). These quasi-isotropic density motifs suggest that the effective ground-state structure of N<sub>2</sub>·N<sub>2</sub> is qualitatively dissimilar to the planar, Z-shaped global minimum. These non-trivial features observed imply in themselves that the N<sub>2</sub>·N<sub>2</sub> dimer fulfills quasistructurality criteria (ii) and (iii).

In panel Fig. 4(c), the four minimum-like features correspond to the four versions<sup>79</sup> of the planar Z-shaped form of the <sup>14</sup>N<sub>2</sub>·<sup>14</sup>N<sub>2</sub> dimer. This suggests that our understanding of the complicated energy and density patterns can be enhanced by a model calculation which artificially localizes the vibrational eigenfunctions around one of the four equivalent Z-shaped versions. In this ‘artificial localization model’, whose precise definition is provided in Section ‘Methods’, each vibrational state becomes four-fold degenerate.

The ground-state density distributions of the localized states of the four Z-shaped versions are shown in Fig. 6. In accordance with the torsion angles, the  $(R, \phi)$  densities are concentrated around  $\phi = 0^\circ$  [Fig. 6(a)] and  $\phi = 180^\circ$  [Fig. 6(b)] for versions I/IV and II/III, respectively. As expected, the artificial localization model gives much simpler density patterns than those seen in Fig. 5. This holds for the excited vibrational states, as well, whose density distributions are not given here.

Figure 7 (a) shows the energy-level structure of the artificial localization model, where the energies are relative to the true vibrational ground state of <sup>14</sup>N<sub>2</sub>·<sup>14</sup>N<sub>2</sub>. As apparent from Fig. 7(b), the first three vibrational states of <sup>14</sup>N<sub>2</sub>·<sup>14</sup>N<sub>2</sub>, of  $A_1^+$ ,  $E^+$ , and  $B_1^+$  symmetry, are reproduced, with a squared overlap of  $\approx 75\%$ , by the signed sums of the four artificially localized ground-state eigenfunctions (the remaining 25 % comes from several excited vibrational states). Basically the same holds for the antisymmetric bend shown in Fig. 7(d), with symmetry species  $B_2^+$ ,  $E^+$ , and  $A_2^+$ . This simple model is unable to explain Fig. 7(c), (e), and (f), whereby further states, indicated with bracketed asterisks, mix in. Excluding these extra states from consideration, the retained state triplets fully reproduce the degeneracy factor of the states illustrated in Fig. 7(c), (e), and (f). Overall, these results yield clear evidence that quasistructurality criteria (iii) and (iv) are satisfied for N<sub>2</sub>·N<sub>2</sub>.

**Strong rovibrational couplings.** For semirigid molecules, separation of the vibrational and rotational degrees of freedom works extremely well for at least the ground vibrational state and the fundamentals, as the vibrational and rotational excitation energies are drastically different, often by more than an order of magnitude. This is not true for the N<sub>2</sub> dimer. The lowest-lying bound vibrational ( $J = 0$ ) states of <sup>14</sup>N<sub>2</sub>·<sup>14</sup>N<sub>2</sub> have energies of only a few cm<sup>-1</sup>, and there are four excited vibrational states with energies less than 10 cm<sup>-1</sup> [see Fig. 7(b)–(d)]. Therefore, these vibrational states can couple effectively with the rotational states, as  $A_{eq}$  is close to 2 cm<sup>-1</sup> for <sup>14</sup>N<sub>2</sub>·<sup>14</sup>N<sub>2</sub> (for the three rotational constants of the Z-shaped global minimum, as well as the other symbols used in this subsection, see the central panel of Fig. 8). Extremely strong coupling between vibrations and rotations, starting at the lowest rotational excitation, has been identified in several neutral and charged molecular systems<sup>80,88–94</sup>. As shown next, similar interactions, which are signs of quasistructural behavior, are present in <sup>14</sup>N<sub>2</sub>·<sup>14</sup>N<sub>2</sub>, as well.

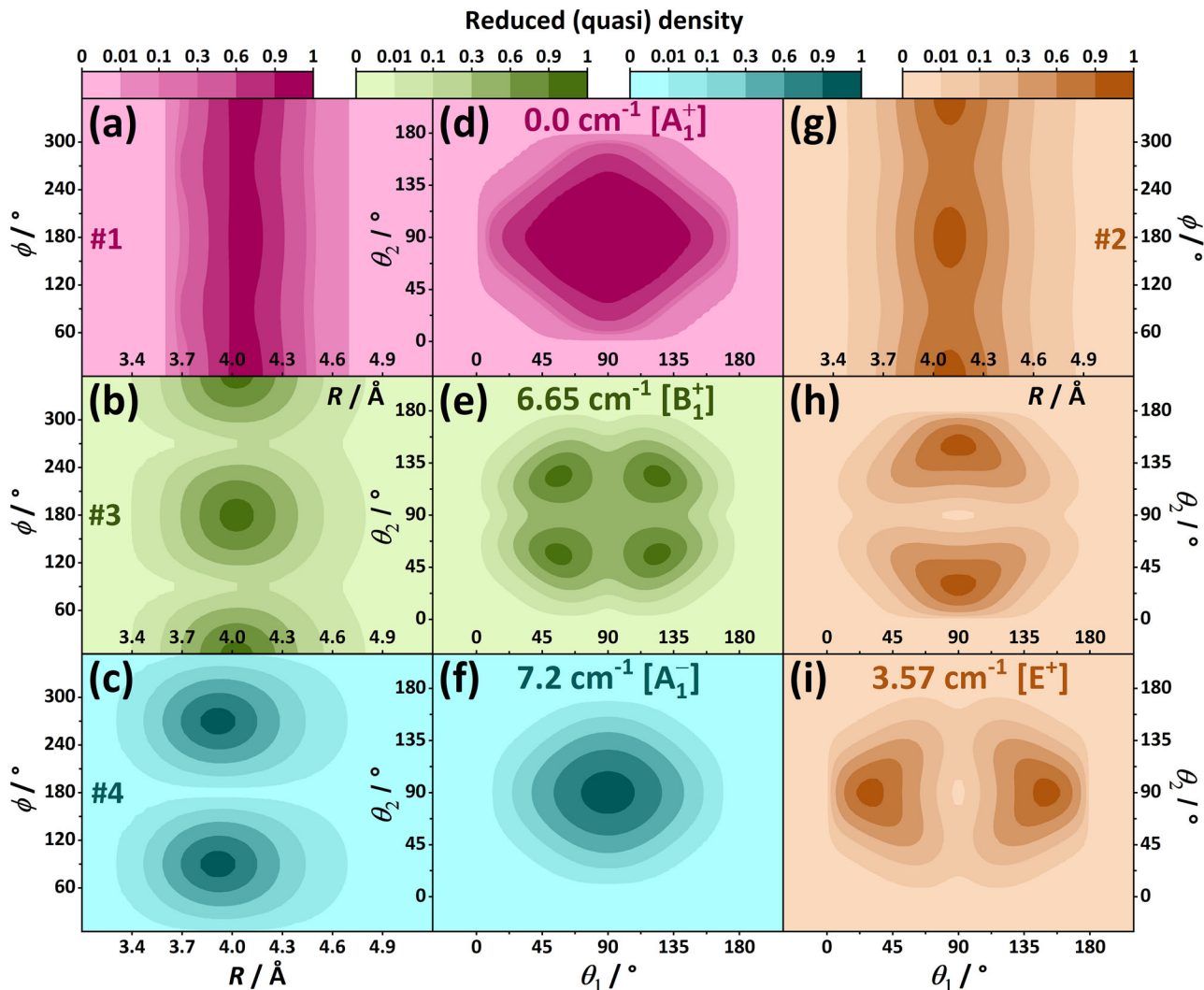


**Fig. 5 | Probability-density distributions for the first four vibrational states of the  $^{14}\text{N}_2 \cdot ^{14}\text{N}_2$  complex.** Panels with identical background color refer to the same state. The #n symbol is the unique serial number of a vibrational state (in an increasing energy order, counting the  $E^+$  state once). The symmetry labels, as well as the

quantum-state energies are indicated once for each state. The  $(R, \phi)$  distribution is identical for the two components of the  $E^+$  state. The reduced (quasi) density is calculated as the sum of the squared eigenvector entries (at high grid resolution) for a specific 2D point, without reliance on the quadrature weights.

Figure 8 shows a collection of rovibrational states with low  $J$  and  $K_a$  values, which were subjected to a rigid-rotor decomposition (RRD) analysis<sup>95</sup>, where  $K_a$  designates the approximate prolate-top rotational quantum number of the asymmetric-top  $^{14}\text{N}_2 \cdot ^{14}\text{N}_2$  dimer. As clear from Fig. 8(a), the rigid-rotor model holds very well for the lowest  $J = 1$  state of  $A_2^-$  symmetry, as  $B_{\text{eq}} + C_{\text{eq}} = 0.142 \approx 0.144 \text{ cm}^{-1}$ , the energy of this state. Thus, the parent vibrational state of this  $J = 1$  rovibrational state can be safely given as the ground vibrational state. On the other hand, Fig. 8(b) and (c) show the breakdown of the rigid-rotor model, as more than half of the vibrational contributions come from excited vibrational states for both the second and third  $J = 1$  rovibrational states at  $3.459$  and  $3.538 \text{ cm}^{-1}$ , respectively. For the rotational energies of these formally “ $1_{1,1}$ ” [ $E^-$ ] and “ $1_{1,0}$ ” [ $E^+$ ] states, the rigid-rotor model provides significantly different values, with  $A_{\text{eq}} + C_{\text{eq}} = 1.837 \text{ cm}^{-1}$  and  $A_{\text{eq}} + B_{\text{eq}} = 1.839 \text{ cm}^{-1}$ , respectively. Thus, in the case of  $^{14}\text{N}_2 \cdot ^{14}\text{N}_2$ , the formal separation of the vibrational and rotational degrees of freedom leads to qualitatively incorrect energies and unacceptable assignment attempts even in the case of the lowest rovibrational states. These are clear signs of quasistructural behavior.

The bottom two panels of Fig. 8 demonstrate how the rotational energies vary, as a function of the  $J$  values, in the rigid-rotor and the variational 4D0 models (note the inverted vertical and horizontal axes). As to

the  $J_{0,J}$  states [green curves in Fig. 8(d) and (e)], the results of the two models follow the same quadratic polynomial trend (see the central panel of Fig. 8 for the parameters of the fitted polynomial). As to the  $J_{1,J-1}$  and  $J_{1,J}$  states, the trends are still quadratic, but the linear and constant terms are considerably different for the two datasets.

With a Ray asymmetry parameter of  $\kappa \approx -0.997$  (see the central panel of Fig. 8), the equilibrium structure of  $^{14}\text{N}_2 \cdot ^{14}\text{N}_2$  corresponds to a nearly prolate symmetric top; thus, the rigid-rotor model predicts fairly small splittings for the  $J_{1,J-1}$  and  $J_{1,J}$  states. In contrast, the variationally computed splittings significantly grow towards larger  $J$  values, indicating increased rovibrational coupling as  $J$  increases. While the symmetric-top quantum number  $K$ , which corresponds to  $K_a$  for prolate symmetric tops, may behave as a nearly good quantum number even for vdW dimers<sup>96,97</sup>, this is seemingly not the case for  $(\text{N}_2)_2$ .

As shown in Fig. 8(b), there is considerable coupling between the  $K_a = 0$  and  $K_a = 1$  rigid-rotor eigenfunctions even for  $J = 1$ , a feature documented neither in ref. 66 nor in refs. 77 and 78. For further insight into the rovibrational mixings present in  $^{14}\text{N}_2 \cdot ^{14}\text{N}_2$ , see the RRD files given in an external repository<sup>86</sup>. In the  $J = 3$  case, where most of the states exhibit pronounced  $K_a$  mixings, the RRD coefficients have been determined using both the N2d-CC and the N2d-H0B PESs, revealing typical deviations on the order of only

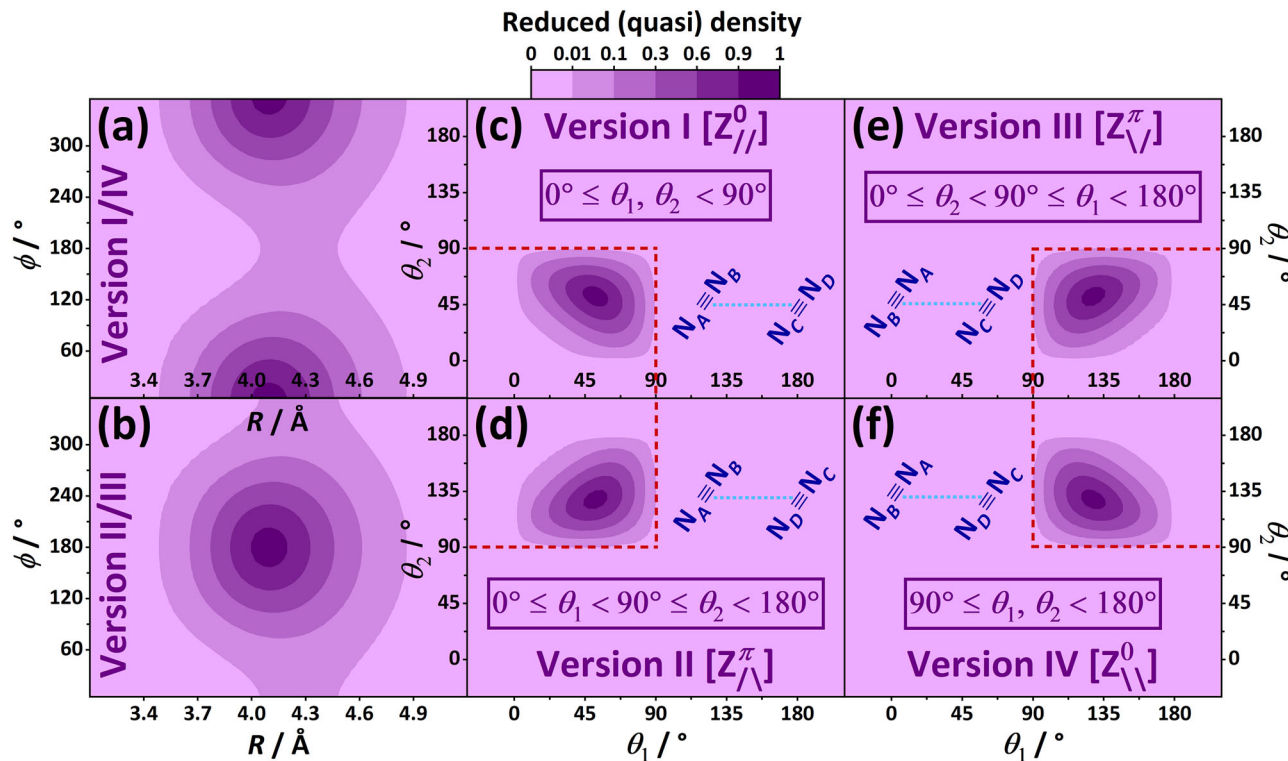


**Fig. 6 | Ground-state density distributions derived for the artificial localization model.** **a, b** and **c–f** show the  $(R, \phi)$  and  $(\theta_1, \theta_2)$  localized density plots of the four Z-shaped versions, respectively. The naming convention applied for these versions are the same as in Fig. 4. For specific details about these plots, consult the caption to Fig. 5. The densities of these four versions are localized in coordinate

regions specified in the violet boxes. Note that these versions with the same torsion angle, namely  $Z_{//}^0$  &  $Z_{//}^\pi$  and  $Z_{\backslash\backslash}^\pi$  &  $Z_{\backslash\backslash}^0$ , are characterized by identical  $(R, \phi)$  density plots, as seen in **(a, b)**, respectively. The schematic representation of the four Z-shaped versions is given in dark blue on **(c–f)**, where  $N_A \equiv N_B$  and  $N_C \equiv N_D$  denote the monomers.

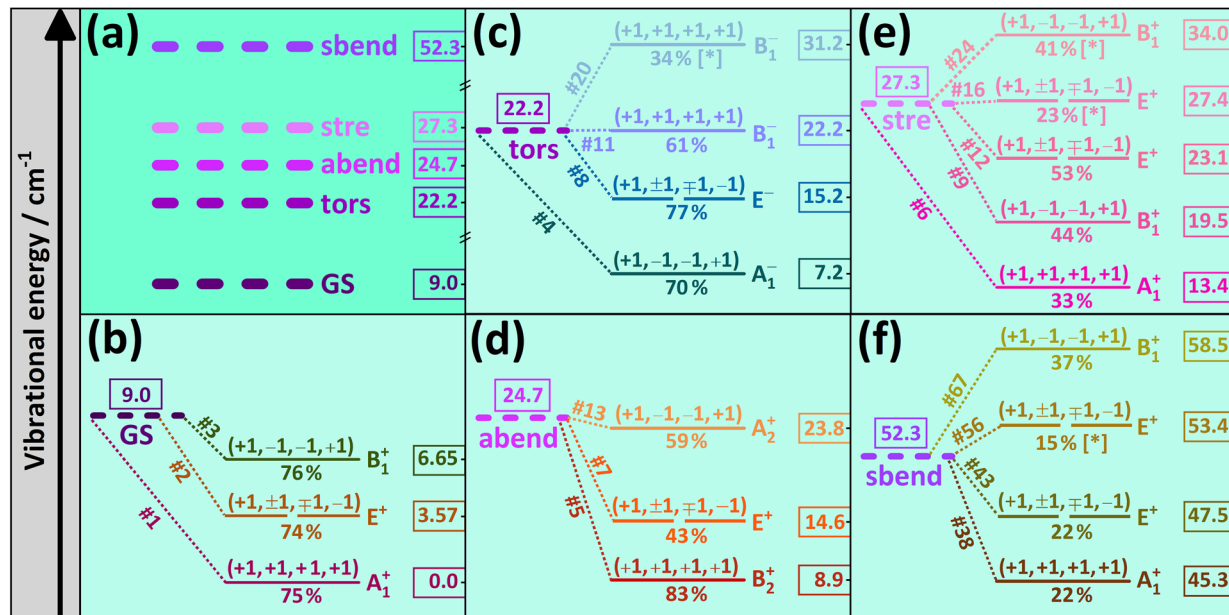


**Fig. 7 | Correspondence of the vibrational states of  $^{14}\text{N}_2\cdot^{14}\text{N}_2$  with those of the artificial localization model.** **a** shows the energies of five vibrational states of the artificial localization model of Section “Models”. These artificially localized states correspond to the ground vibrational state (GS), the torsional (tors), the antisymmetric bend (abend), the intermonomer stretch (stre), and the symmetric bend (sbend) fundamentals. **b–f** display each vibrational state of  $^{14}\text{N}_2\cdot^{14}\text{N}_2$  whose wave function expansion, specified in Eq. (7), contains the largest contribution from one of the states of **(a)**. Symbol  $\#n$  has the same meaning as in Fig. 5. In each panel, the energy values are placed into colored boxes. These vibrational energies, given in

$\text{cm}^{-1}$ , are relative to that of state  $\#1$  in **(b)**. The individual states are illustrated with horizontal lines, where the number of dashes corresponds to their degeneracy factor. The states are distributed according to the right-hand-side vertical energy axes (note the several axis breaks). A sign quadruplet, e.g.,  $(+1, +1, +1, +1)$  for the GS, serves as an assignment of a vibrational state, and contains the signs attached to the most dominant contribution according to Eq. (7). The squared coefficients of these dominant terms are given as percentages. The asterisks in brackets highlight the “extra” states which break the four-fold overall degeneracy of the artificial localization model.

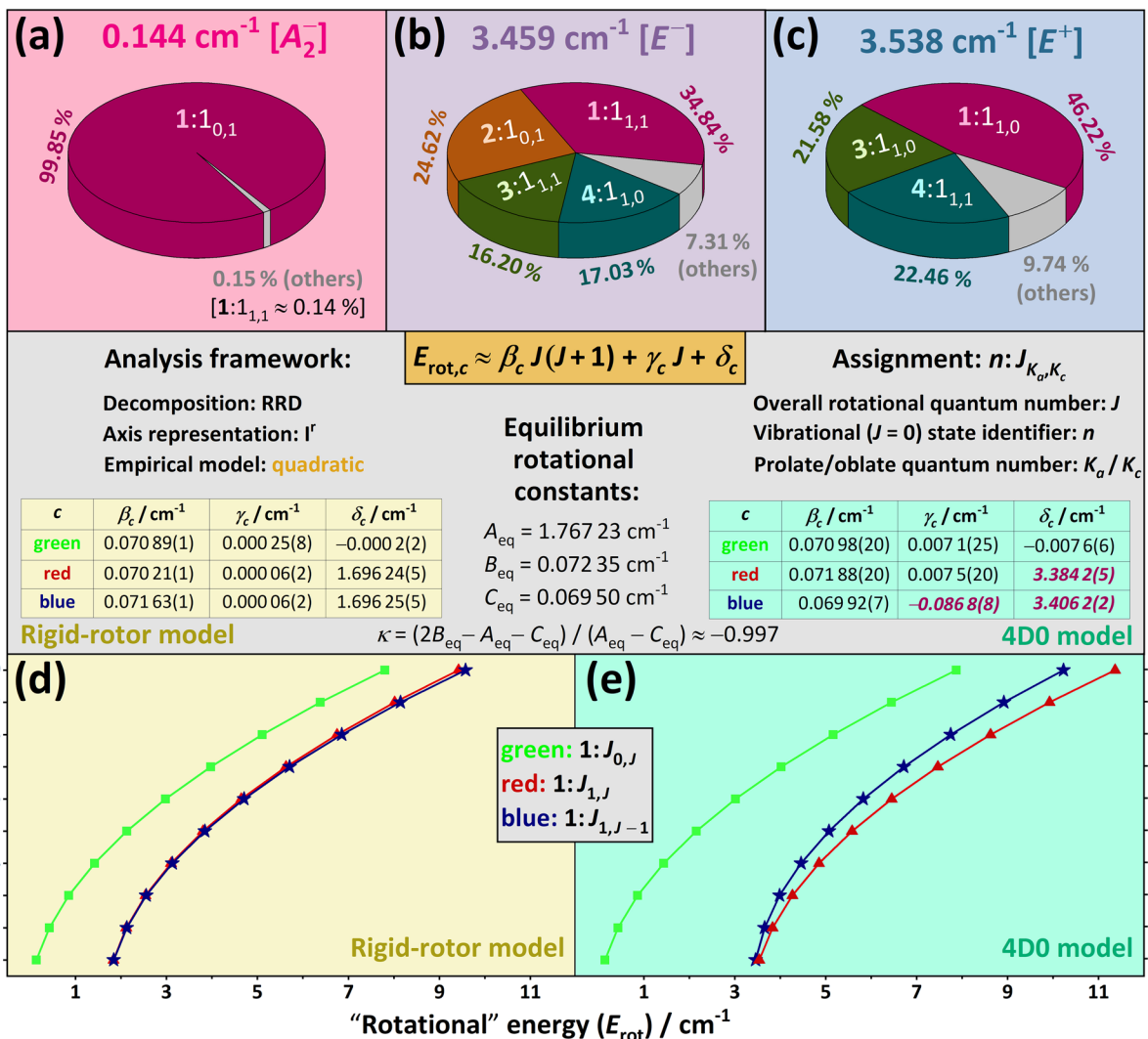


**Fig. 8 | Illustration of the strong rovibrational couplings in selected rovibrational states of the  $^{14}\text{N}_2 \cdot ^{14}\text{N}_2$  complex.** The pie charts of (a–c) demonstrate the results obtained for the lowest three  $J = 1$  states, using the rigid-rotor decomposition (RRD) method<sup>95</sup> and the  $I'$  axis representation<sup>120</sup>. The percentages on (a–c) are squared overlaps among the true eigenstates and the products of the pure vibrational ( $J = 0$ ) and the rigid-rotor (RR) eigenstates [the assignments of these products are defined in the central panel]. The RRD contributions coming from the two eigenvectors of the degenerate eigensubspaces are summed up in the percentages. Notice that the same colors are used here and in Fig. 5 to denote the vibrational states. For all the bound rovibrational states computed during this study, the mixing coefficients form part of

an external repository<sup>86</sup>. d, e describe the  $J$  dependence of the lowest three rovibrational energies in the RR and the variational (4D0) models, respectively (for simplicity, the horizontal and vertical axes are swapped). For these two datasets, a quadratic model was fitted, whose parameters, along with their last-few-digit (two-sigma) uncertainties in parentheses are given in the central panel. The rotational constants of the Z-shaped global minimum, derived from the N2d-CC PES, as well as its Ray asymmetry constant  $\kappa$ <sup>79</sup>, are also reported in the central panel. Those fitted parameters of the 4D0 dataset which differ considerably from their RR counterparts are typeset in purple bold italics.

1–2 %. This means that the mixing appears to be a genuine physical effect rather than an artifact due to the analytical PESs employed.

Performing a global fit to all of the  $J \leq 10$  bound rovibrational states where the ground vibrational state gives the dominant RRD contribution, the following empirical model, not shown in Fig. 8, was obtained (for improved transparency, the  $\pm$  notation is used here to display the two-sigma uncertainties of the parameters):

$$E_{\text{rot}}(J, K_a) / \text{cm}^{-1} = (0.071 \pm 0.002) J(J+1) + (1.95 \pm 0.02) K_a^2 + (1.5 \pm 0.1) K_a \quad (2)$$

Note the importance of the inclusion of the term linear in  $K_a$  in the energy expression. In our previous studies on  $\text{CH}_4 \cdot \text{F}$ <sup>88</sup> and  $\text{H}_5^+$ <sup>89</sup>, due to the strong coupling between the vibrational and rotational degrees of freedom, a term linear in  $K$  was also shown to have a remarkable impact on the rotational-rovibrational energy level pattern. Clearly, the discussion presented above

about the various aspects of the coupling of rotations and vibrations provides further evidence that  $\text{N}_2 \cdot \text{N}_2$  satisfies quasistructurality criteria (iii) and (v).

### Concluding remarks

Non-covalent interactions govern the dynamical behavior and properties of numerous molecular systems; thus, their detailed understanding is of extreme importance when studying weakly-bound molecular systems, however small or large these interactions are. In this work, the structure, nuclear dynamics, and rovibrational states of the prototypical van der Waals (vdW) dimer,  $\text{N}_2 \cdot \text{N}_2$ , have been investigated. Our computational study relied on two newly created full-dimensional potential energy surfaces, designed with spectroscopic ( $\approx 1 \text{ cm}^{-1}$ ) accuracy in mind.

Symmetry-adapted variational solution of the nuclear Schrödinger equation resulted in some 6000 bound rovibrational states for the parent  $^{14}\text{N}_2 \cdot ^{14}\text{N}_2$  isotopologue up to  $J = 10$ , where  $J$  is the

**Table 4 | The internal coordinates adopted in this study to describe the molecular structure of the N<sub>2</sub> dimer<sup>(a)</sup>**

Internal coordinate			DVR	Model <sup>(g)</sup>				
Label	Definition <sup>(b)</sup>	Range <sup>(c)</sup>	Type <sup>(e)</sup>	Size <sup>(f)</sup>	6D	4D	4D0	2D
$r_1$	stre(N <sub>1</sub> ', N <sub>1</sub> '')	[0.9 Å, 1.3 Å]	PO-Laguerre <sup>121,122</sup>	6/6	A	F{Z}	F{Z0}	A
$r_2$	stre(N <sub>2</sub> ', N <sub>2</sub> '')	[0.9 Å, 1.3 Å]	PO-Laguerre <sup>121,122</sup>	6/6	A	F{Z}	F{Z0}	A
$R$	stre(COM <sub>1</sub> , COM <sub>2</sub> )	[3.3 Å, 8.4 Å] <sup>(d)</sup>	Hermite <sup>122</sup>	45/6	A	A	A	F{Z}
$\theta_1$	bend(N <sub>1</sub> ', COM <sub>1</sub> , COM <sub>2</sub> )	(0, $\pi$ )	cotangent <sup>117</sup>	14/12	A	A	A	F{Z}
$\theta_2$	bend(N <sub>2</sub> ', COM <sub>2</sub> , COM <sub>1</sub> )	(0, $\pi$ )	cotangent <sup>117</sup>	14/12	A	A	A	F{Z}
$\phi$	tors(N <sub>1</sub> ', COM <sub>1</sub> , COM <sub>2</sub> , N <sub>2</sub> ')	[0, 2 $\pi$ )	exponential <sup>123–125</sup>	12/8	A	A	A	F{Z}

<sup>(a)</sup>The coordinates are defined for a distinguished version<sup>79</sup> of the N<sub>2</sub> dimer, with its two monomers N<sub>1</sub>' ≡ N<sub>1</sub>'' and N<sub>2</sub>' ≡ N<sub>2</sub>'', whose centers of mass are COM<sub>1</sub> and COM<sub>2</sub>, respectively. These sites specify the right-handed embedding chosen in this study, where (i) COM<sub>2</sub> COM<sub>1</sub> is the direction vector of the z axis, (ii) N<sub>1</sub>' lies on the positive x-side of the xz plane, and (iii) the origin is shifted to the dimer's COM.

<sup>(b)</sup>The definition of the internal coordinates uses the standard abbreviations "stre", "bend", and "tors", corresponding to stretching, bending, and torsional coordinates, respectively<sup>100</sup>, which depend on the positions of the sites listed in parentheses.

<sup>(c)</sup>Coordinate ranges applied for the coordinates, optimized for the variational nuclear-motion computations of this study.

<sup>(d)</sup>For the two intramonomer stretch fundamentals, the  $R$  range could be reduced to [3.6, 4.7] Å.

<sup>(e)</sup>Discrete variable representation (DVR) basis types applied during our first-principles nuclear-motion computations. The prefix "PO-" means that potential optimization<sup>121</sup> was employed for the underlying grid points with the help of a 1D model.

<sup>(f)</sup>Optimal DVR sizes for the bound/resonance states, separated by slashes.

<sup>(g)</sup>Dynamical models with active/frozen coordinates designated as A/F. Coordinates with "F{Z}" are frozen at their values within the Z-shaped global minimum. In the 4D0 model, "F{Z0}" means that a vibrationally averaged N ≡ N ("r<sub>0</sub>") bond length is used for the fixed coordinates rather than the equilibrium bond lengths of the Z-shaped form. To obtain  $r_0$  values for the two new PESs, a vibrational correction, estimated as  $\delta r_0 = 0.0037$  Å<sup>72</sup>, was added to the equilibrium bond lengths.

rotational quantum number. Following the recommendations of ref. 52 and a recent review on reporting spectroscopic data<sup>98</sup>, individual uncertainty estimates, with a median value of 0.8 cm<sup>-1</sup>, are also reported for each state, along with symmetry labels corresponding to the irreducible representations of the  $G_{16}$  molecular symmetry group. Accurate shifts and splittings have been determined for the quasi-bound intramonomer stretch fundamentals, as it is expected that the yet missing experimental results can be most easily generated in this spectral region. Isotope effects have also been considered for the lowest excited vibrational states of N<sub>2</sub>·N<sub>2</sub>, where the shifts and splittings computed were perfectly explained by a simple bilinear model.

Based on the extensive computational results of this study and the thorough analysis of the intriguing structural/dynamical features observed, it has been firmly established that N<sub>2</sub>·N<sub>2</sub> is a quasistructural species, whereby, for example, considerable mixing can be observed in the lowest-energy rovibrational quantum states among the four versions of its Z-shaped global minimum. Similar vdW dimers are expected to fall into the class of quasistructural systems, meaning that the interpretation of their observed high-resolution spectra would require a special view of their nuclear motion and molecular structure.

## Methods

### Internal coordinates and nuclear-motion models

During the present study, the nuclear motions of the nitrogen dimer, N<sub>2</sub>·N<sub>2</sub>, have been represented with the six curvilinear internal coordinates given in the first two columns of Table 4, whereby the functions stre(·, ·), bend(·, ·, ·), and tors(·, ·, ·, ·) follow the conventional definitions of bond lengths, bond angles, and torsion angles, respectively<sup>99,100</sup>. This internal-coordinate system is ill-defined for  $\theta_2 \in \{0, \pi\}$ : in that case,  $\phi$  is arbitrary and thus one can set  $\phi = 0$ . The last four columns of Table 4, under 'Model', contain information about the utilization of the internal coordinates during the solution of the time-independent nuclear-motion Schrödinger equation (see Section "Symmetry-adapted variational nuclear-motion computations"). The 6D, 4D, 4D0, and 2D models are defined by a collection of active/frozen (A/F) coordinates, as well as by the values where the frozen coordinates are fixed.

### Electronic-structure computations

The electronic-structure computations of this study have been performed at the Hartree–Fock, MP2, SAPT, and coupled-cluster levels (up to perturbative pentuple excitations in the latter case), utilizing Dunning's aug-cc-

pVQZ basis sets<sup>101</sup> up to X = 6. These computational results form the basis of an FPA analysis<sup>49,51</sup>, and they helped to construct two full-dimensional PESs for the N<sub>2</sub> dimer at the "CC" and "SAPT" levels (see Table 5). The "SAPT" protocol corresponds to a density-fitted SAPT(DFT) scheme<sup>102–104</sup>, where the PBE0<sup>105</sup> functional is adopted, alongside the aug-cc-pVQZ basis set<sup>101</sup>, to describe the electronic structure of the isolated N<sub>2</sub> monomer. The "CC" approach represents counterpoise-corrected, frozen-core CCSD(T), where a CBS extrapolation is carried out using the aug-cc-pVTZ and aug-cc-pVQZ basis sets<sup>101</sup> plus midbond functions<sup>106</sup>. Within the "CC" scheme, the Hartree–Fock and the correlation terms were extrapolated *via* formulas reported in refs. 94 and 107, respectively.

The comparisons given in Fig. 1 are based on Hellmann's direct electronic-structure computations<sup>72</sup>. Hellmann published reference (intermonomer) interaction energies for 408 dimer configurations, keeping the two intramonomer distances fixed at the vibrationally averaged ("r<sub>0</sub>") bond length of the isolated N<sub>2</sub> molecule. Among the different levels considered by Hellmann, the highest one is what is abbreviated here as H0B (≡ Hellmann's  $r_0$ -based benchmark scheme), which includes perturbative quadruples [(Q)], counterpoise, core–core plus core–valence, and relativistic corrections near the complete basis set (CBS) and full configuration interaction (FCI) limits<sup>33,53</sup>. The (Q) correction is indeed the highest-order coupled-cluster term which can be afforded for hundreds of dimer arrangements using a reasonable basis set. In the H0B energy values, Hellmann applied a scaling factor of 0.5 for the (Q) corrections to increase the accuracy of virial coefficients yielded by his quasiclassical Monte–Carlo simulations. It turns out, however, from our examination, that the post-CCSD(T) effects do not play a significant role in achieving spectroscopic ( $\approx 1$  cm<sup>-1</sup>) accuracy for the rovibrational states of N<sub>2</sub>·N<sub>2</sub>: this justifies the neglect of the expensive iterative triples and (Q) terms during the determination of the full-dimensional (6D) PESs.

### PES construction

To determine 6D PESs for the N<sub>2</sub> dimer, the autoPES program suite<sup>35,39</sup>, interfaced to SAPT<sup>58</sup>, MOLPRO<sup>108</sup>, and ORCA<sup>109</sup>, was employed, ensuring a highly automatic treatment. To help evaluate the uncertainty of our rovibrational results, two PES versions, named N2d-SAPT and N2d-CC, were created with autoPES, corresponding to the "SAPT" and "CC" levels, respectively (for the specifications of these two computational protocols, see Section "Potential energy surfaces and stationary points"). Concerning the final versions of these two PESs, a few important characteristics, those that guide our description of their generation, are listed in Table 5.

**Table 5 | The main characteristics of the two full-dimensional potential energy surfaces developed during this study<sup>(a)</sup>**

Indicator	N2d-SAPT	N2d-CC
$(z_1^{OA}, z_2^{OA}, z_3^{OA}, z_4^{OA}, z_5^{OA})^{(b)}$	(-0.436, -0.219, 0, 0.219, 0.436)	(-0.676, -0.272, 0, 0.272, 0.676)
range( $r_{1/2}$ ) <sup>(c)</sup>	[-0.08, 0.10] + 1.088 83 <sup>(d)</sup>	[-0.09, 0.09] + 1.098 66 <sup>(d)</sup>
range( $R$ ) <sup>(c)</sup>	[2.5, 8.4]	[2.7, 8.4]
range( $\Delta E_{int}$ ) <sup>(e)</sup>	[-104.8, 6499]	[-107.4, 9181]
range( $\Delta E_{inter}$ ) <sup>(e)</sup>	[-106.2, 3683]	[-107.4, 5127]
range( $\Delta E_{intra}$ ) <sup>(e)</sup>	[0, 6200]	[0, 9182]
$N_{par}^{(f)}$	113	143
$N_{geo}^{(g,i)}$	171 / 2263 / 2437	172 / 1699 / 1847
RMSD <sup>(h,i)</sup>	0.48 / 0.64 / 0.62	0.18 / 0.23 / 0.97

<sup>(a)</sup>The parameters listed here pertain to the final version of the two (N2d-SAPT and N2d-CC) potentials, relying on a new sampling scheme described in Supplementary Note 2.

<sup>(b)</sup>Positions of the five off-atomic (OA) sites, specified in Å, alongside the z axis; that is, the symmetry axis of the isolated N<sub>2</sub> monomer, whose center of mass (COM) corresponds to (x, y, z) = (0, 0, 0).

<sup>(c)</sup>Ranges of the radial ( $r_1$  and  $r_2$ , and  $R$ ) coordinates within the fitting dataset, given in Å.

<sup>(d)</sup>Equilibrium N ≡ N bond lengths of the isolated N<sub>2</sub> molecule derived from the two PESs.

<sup>(e)</sup>Ranges of the interaction energies and their (intra/inter)monomer contributions, in cm<sup>-1</sup>, within the fitting dataset.

<sup>(f)</sup>Number of parameters used in the intermonomer fit. Beyond them, 13 parameters were also employed in the intramonomer fit to reproduce the Rydberg–Klein–Rees potential of the isolated N<sub>2</sub> monomer.

<sup>(g)</sup>Number of dimer geometries generated by the sampling process for the intermonomer fit.

<sup>(h)</sup>Root-mean-square deviations (RMSD), in cm<sup>-1</sup>, characterizing the intermonomer fit.

<sup>(i)</sup>These rows comprise data triplets separated by slashes, representing two distinguished subsets of grid points, subsets I and II, and the whole grid set. Subset I contains geometries with negative interaction energies, while subset II includes those configurations whose probability-density-based weights are not smaller than 0.1 [for this weighting scheme, see Supplementary Note 2].

To enhance the flexibility of our fitted 6D PESs, five off-atomic (OA) sites were introduced for both monomers: one at its center of mass (COM) and two others on the two sides of the COM along the principal symmetry axis. The OA positions were optimized with the PES parameters, forcing them to preserve the monomer's  $D_{\infty h}$  point-group symmetry. Permutation invariance of the PESs was maintained by introducing a common set of parameters for the four nitrogen atoms of the N<sub>2</sub> monomers. Under these constraints, the interaction energies were treated as the sums of the intramonomer (deformation) and intermonomer energies:

$$\Delta E_{int}(r_1, r_2, \rho) = \Delta E_{intra}(r_1, r_2) + \Delta E_{inter}(r_1, r_2, \rho), \quad (3)$$

where  $\rho = (R, \theta_1, \theta_2, \phi)^T$  designates the intermonomer ("relative") coordinates of the N<sub>2</sub> dimer, with the restriction that  $\Delta E_{intra}(r_e, r_e) = 0$  and  $\lim_{R \rightarrow \infty} \Delta E_{inter}(r_1, r_2, \rho) = 0$  ( $r_e$  symbolizes the equilibrium bond length of the isolated N<sub>2</sub> molecule at the "CC"/"SAPT" level). The term  $\Delta E_{inter}(r_1, r_2, \rho)$  is based on damped interaction (exponential, Coulombic, induction + dispersion, and polarization) models<sup>35,39</sup>, while the  $\Delta E_{intra}(r_1, r_2)$  contribution is fitted as a sum of two-body polynomials<sup>39</sup> in a separate phase, trained on "experimental" (Rydberg–Klein–Rees) deformation-energy values<sup>1,110</sup> (see also Supplementary Note 2).

The intermonomer fitting process was divided into two parts, based on separate short- ( $R \leq 7$  Å) and long-range ( $R > 7$  Å) configuration spaces. In the short-range regime, the intermonomer energies of the grid points were determined at the "SAPT" and "CC" levels. In the long-range domain, where the accuracy requirement is less stringent, the intermonomer energies were computed for 9000 grid points with a multipole expansion along the  $R$  coordinate (see refs. 35 and 111). To produce preliminary versions for the N2d-SAPT/CC PESs, the standard built-in algorithms of the autoPES code were employed during the grid-generation and the PES-parametrization process (see Secs. II–IV of ref. 39). This procedure was performed according to an iterative (grid generation – fitting – identification

of minima – hole fixing) scheme, until a reliable intermonomer fit was obtained.

After computing the two intramonomer stretch fundamentals for N<sub>2</sub>·N<sub>2</sub>, it has become apparent that the accuracy/stability of their splitting tends to be limited across the intermediate versions of the N2d-CC/SAPT PESs. This may be due to the fact that autoPES focuses mostly on the lower-energy ( $\Delta E_{int} < 0$ ) region of the "CC"/"SAPT" PES while sampling the grid points and weighting the fitted data. Thus, a new grid-sampling and weighting scheme has been implemented in autoPES, using direct-product-based wave-function coefficients to define point-by-point weights (this method is akin to density-guided PES sampling advocated in ref. 112). A couple of important details about this new protocol, called amplitude-driven sampling (ADS), are provided in Supplementary Note 2. These modified weights, in combination with ADS, led to accurate N2d-CC/SAPT PESs, enabling us to compute (a) rovibrational energies for N<sub>2</sub>·N<sub>2</sub> with an uncertainty of 0.5–1.5 cm<sup>-1</sup>, and (b) the shifts/splittings of the N ≡ N stretch fundamentals with an accuracy of  $\pm 0.1$  cm<sup>-1</sup> (for details, see Section "First-principles rovibrational results").

### Symmetry-adapted variational nuclear-motion computations

When breaking the monomer bonds is not allowed, the quantum states of the N<sub>2</sub>·N<sub>2</sub> isotopologues comprising four identical isotopes transform according to the irreducible representations (irreps) of the  $G_{16}$  molecular symmetry (MS) group<sup>79,113</sup>. The 16 distinct symmetry operations of the  $G_{16}$  group<sup>79,113</sup> can be expressed as products of three elementary operations,  $\mathcal{E}^*$ ,  $\mathcal{P}_1$ , and  $\mathcal{P}_{12}$ , where  $\mathcal{E}^*$  is the space-inversion operation,  $\mathcal{P}_1$  is a permutation within monomer 1, and  $\mathcal{P}_{12}$  represents the permutation that interchanges the two monomers. The character table of the  $G_{16}$  group, with the ten irreps denoted as  $A_{1/2}^{\pm}$ ,  $B_{1/2}^{\pm}$ , and  $E^{\pm}$ , is given in Table A-25 of ref. 79 (note that our study uses the Merer–Watson convention<sup>114</sup> for the irreps). For this group, the selection rules for the dipole-allowed transitions are  $A_1^{\pm} \leftrightarrow B_1^{\mp}$ ,  $A_2^{\pm} \leftrightarrow B_2^{\mp}$ , and  $E^{\pm} \leftrightarrow E^{\mp}$ <sup>66,78,113</sup>. Note that the N<sub>2</sub>·N<sub>2</sub> isotopologues containing non-identical nuclei belong to different subgroups of  $G_{16}$ .

As nuclear spins are not considered explicitly during the solution of the time-independent nuclear Schrödinger equation, their effects must be taken into account *a posteriori*. Since <sup>14</sup>N is a spin-1 nucleus, the monomers of the <sup>14</sup>N<sub>2</sub>·<sup>14</sup>N<sub>2</sub> isotopologue co-exist in separate *ortho* and *para* forms (with total nuclear spins 0/2 and 1, respectively). Thus, the rovibrational states of <sup>14</sup>N<sub>2</sub>·<sup>14</sup>N<sub>2</sub> can be divided into three sets: *ortho*–*ortho* ( $A_1^+$ ,  $A_2^-$ ,  $B_1^-$ , and  $B_2^+$ ), *para*–*para* ( $A_1^-$ ,  $A_2^+$ ,  $B_1^+$ , and  $B_2^-$ ), and *ortho*–*para* ( $E^+$  and  $E^-$ )<sup>66,78,113</sup>. Since the nuclear-spin weights have nonzero values for all irreps of  $G_{16}$ <sup>113</sup>, there are no missing symmetry blocks for <sup>14</sup>N<sub>2</sub>·<sup>14</sup>N<sub>2</sub> (in other words, all computed quantum states exist). The same holds for all the other isotopologues of the N<sub>2</sub> dimer given in Table 3, with the exception of <sup>15</sup>N<sub>2</sub> · <sup>15</sup>N<sub>2</sub>, where the  $A_2^-$  and  $B_2^+$  states do not exist.

Achieving converged rovibrational results required a large number of symmetry-adapted<sup>92</sup> computations with the code GENIUSH<sup>115,116</sup>, used for the variational-like solution of the nuclear Schrödinger equation in both full and reduced dimensions. In these computations, the masses of the <sup>14</sup>N and <sup>15</sup>N nuclei were set to 14.003 074 and 15.000 109 u, respectively. The optimal discrete variable representation (DVR) basis sizes and radial-coordinate ranges, see Table 4, were selected so that all the vibrational energies reported are converged to within 0.02 cm<sup>-1</sup> (for the two intramonomer stretch fundamentals, their shifts and splittings were also monitored, attaining a computational precision of 0.002 cm<sup>-1</sup>). Convergence of the two bending basis sets was significantly accelerated by using the cotangent DVR scheme<sup>117</sup>, which yields much smoother variations for the computed eigenvalues than the traditional Legendre-DVR basis<sup>118,119</sup>. Note that FBR (finite basis representation) basis sets exhibit better convergence for dimers of linear molecules<sup>66,77,78</sup>. In practice, though, FBR requires handling complicated, non-sparse potential-energy matrices, unlike DVR, where the potential matrix is diagonal. For further details, see Supplementary Note 3, as well as an external repository<sup>86</sup>, where the results of our convergence tests are placed in a folder called "conv\_tests".

Rovibrational energies have been computed with the aid of the following three PESs: N2d-H0B, N2d-SAPT, and N2d-CC. The computed energy values,  $e_p^{[J]}$ , have an associated expanded (two-sigma) uncertainty,  $U^{[J]}$ . The  $e_p^{[J=0]}$  energies are deduced from a 6D model, whose uncertainties are estimated as

$$U^{[J=0]} = |e_{\text{N2d-CC}}^{[J=0]}(4\text{D0}) - e_{\text{N2d-H0B}}^{[J=0]}(4\text{D0})| + |\delta e_{\text{N2d-CC}}^{[J=0]}(6\text{D}) - \delta e_{\text{N2d-SAPT}}^{[J=0]}(6\text{D})|, \quad (4)$$

where  $e_p^{[J]}(m)$  designates the rovibrational energy at a given  $J$  value, corresponding to PES version  $p$  and model dimensionality  $m$ , and  $\delta e_p^{[J]}(6\text{D}) = e_p^{[J]}(6\text{D}) - e_p^{[J]}(4\text{D0})$  is the 6D correction to the 4D0 rovibrational energy. For  $J > 0$ , only 4D0 computations have been made, leading to expanded uncertainties approximated as

$$U^{[J > 0]} = |e_{\text{N2d-CC}}^{[J > 0]}(4\text{D0}) - e_{\text{N2d-H0B}}^{[J > 0]}(4\text{D0})| + \alpha_{\text{max}} e_{\text{N2d-CC}}^{[J > 0]}(4\text{D0}), \quad (5)$$

where  $\alpha_{\text{max}} = 0.64\%$  is the maximum value of an adjustment factor,

$$\alpha = \left( |\delta e_{\text{N2d-CC}}^{[J=0]}(6\text{D}) - \delta e_{\text{N2d-SAPT}}^{[J=0]}(6\text{D})| + |\delta e_{\text{N2d-CC}}^{[J=0]}(6\text{D})| \right) / e_{\text{N2d-CC}}^{[J=0]}(4\text{D0}), \quad (6)$$

obtained for the vibrational ( $J=0$ ) states (for the  $\alpha$  values, see the “states.xls” file in an external repository<sup>86</sup>). Note that this  $\alpha_{\text{max}}$ -based term is used to describe the energy dependence of the 6D – 4D deviations. Since the PES-related uncertainty is the most dominant contributor to the uncertainties of the computed energies, Eqs. (4)–(6) should provide realistic estimates for these uncertainties.

### The artificial localization model

To define artificially localized eigenstates for each of the four equivalent Z-shaped versions of the  $^{14}\text{N}_2 \cdot ^{14}\text{N}_2$  dimer, the potential energy was drastically increased, to  $0.5 E_h$ , at those direct-product grid points which do not belong to the  $(\theta_1, \theta_2)$  coordinate range of the chosen version (see Fig. 6). This model, which artificially distinguishes the four versions of  $^{14}\text{N}_2 \cdot ^{14}\text{N}_2$ , requires the execution of four nuclear-motion computations. In this model, the wavefunction is excluded from three out of the four  $(\theta_1, \theta_2)$  coordinate quadrants. For each quadruply degenerate state  $v$  of this model, the artificially localized eigenfunctions form an orthonormal quadruplet  $(\Lambda_v^I, \Lambda_v^{II}, \Lambda_v^{III}, \Lambda_v^{IV})$ , where  $\Lambda_v^V$  is the localized eigenfunction of state  $v$  in version  $V$ .

Using the set of eigenfunction quadruplets  $(\Lambda_v^I, \Lambda_v^{II}, \Lambda_v^{III}, \Lambda_v^{IV})$ , a rovibrational state of the  $^{14}\text{N}_2 \cdot ^{14}\text{N}_2$  dimer can be expressed as

$$\psi \approx \sum_v o_v (s_v^I \Lambda_v^I + s_v^{II} \Lambda_v^{II} + s_v^{III} \Lambda_v^{III} + s_v^{IV} \Lambda_v^{IV}), \quad (7)$$

where  $s_v^V = \pm 1$  is a sign associated with the  $(\psi, \Lambda_v^V)$  pair, and  $o_v$  stands for the unsigned wave function overlap between  $\psi$  and  $\Lambda_v^V$ , which are the same for the four Z-shaped versions. Each wave function  $\psi$  can be labelled with (a) the four-fold degenerate state  $v$  having the largest  $o_v$  value, and (b) its sign quadruplet  $(s_v^I, s_v^{II}, s_v^{III}, s_v^{IV})$ . To avoid labeling inconsistencies, the (arbitrary) eigenfunction phases are synchronized by imposing the  $s_v^I = +1$  and  $\Lambda_v^I = \mathcal{P}_2 \Lambda_v^{II} = \mathcal{P}_1 \Lambda_v^{III} = \mathcal{P}_1 \mathcal{P}_2 \Lambda_v^{IV}$  conditions upon each  $v$ , where the  $\mathcal{P}_{1/2}$  operation interchanges the two  $^{14}\text{N}$  nuclei within monomer 1/2.

### Data availability

The computational data obtained during this study are available under the following OSF repository: <https://doi.org/10.17605/OSF.IO/RJ6XB>. This repository consists of two main units: (a) “pots.zip”, which contains FORTRAN implementations of the N2d-H0B, N2d-CC, and N2d-SAPT PESs, as well as (b) “rovib.zip”, a compressed archive of bound-state rovibrational

energies for  $J \leq 10$ , internal-coordinate wavefunction (quasi) densities, rigid-rotor decomposition files, and convergence tests using various basis functions and PESs.

Received: 5 June 2025; Accepted: 17 September 2025;

Published online: 07 November 2025

### References

1. Le Roy, R. J., Huang, Y. & Jary, C. An accurate analytic potential function for ground-state  $\text{N}_2$  from a direct-potential-fit analysis of spectroscopic data. *J. Chem. Phys.* **125**, 164310 (2006).
2. Li, H. & Le Roy, R. J. Quadrupole moment function and absolute infrared quadrupolar intensities for  $\text{N}_2$ . *J. Chem. Phys.* **126**, 224301 (2007).
3. Crawford, M., Welsh, H. & Locke, J. Infrared absorption of oxygen and nitrogen induced by intermolecular forces. *Phys. Rev.* **75**, 1607 (1949).
4. Frommhold, L. *Collision Induced Absorption in Gases* (Cambridge University Press, 2006).
5. Kollman, P. A. Noncovalent interactions. *Acc. Chem. Res.* **10**, 365–371 (1977).
6. Hobza, P. & Müller-Dethlefs, K. *Non-Covalent Interactions: Theory and Experiment* (Royal Society of Chemistry, 2010).
7. Levine, H. B. & Birnbaum, G. Classical theory of collision-induced absorption in rare-gas mixtures. *Phys. Rev.* **154**, 86–92 (1967).
8. Sheng, D. T. & Ewing, G. E. Collision induced infrared absorption of gaseous nitrogen at low temperatures. *J. Chem. Phys.* **55**, 5425–5430 (1971).
9. Long, C. A., Henderson, G. & Ewing, G. E. The infrared spectrum of the  $(\text{N}_2)_2$  van der Waals molecule. *Chem. Phys.* **2**, 485–489 (1973).
10. Buontempo, U., Cunsolo, S., Jacucci, G. & Weis, J. The far infrared absorption spectrum of  $\text{N}_2$  in the gas and liquid phases. *J. Chem. Phys.* **63**, 2570–2576 (1975).
11. Courtin, R. The spectrum of Titan in the far-infrared and microwave regions. *Icarus* **51**, 466–475 (1982).
12. Dagg, I., Anderson, A., Yan, S., Smith, W. & Read, L. Collision-induced absorption in nitrogen at low temperatures. *Can. J. Phys.* **63**, 625–631 (1985).
13. Borysow, A. & Frommhold, L. Collision-induced rototranslational absorption spectra of  $\text{N}_2\text{--N}_2$  pairs for temperatures from 50 to 300 K. *Astrophys. J.* **311**, 1043–1057 (1986).
14. McKellar, A. R. W. Infrared spectra of the  $(\text{N}_2)_2$  and  $\text{N}_2\text{--Ar}$  van der Waals molecules. *J. Chem. Phys.* **88**, 4190–4196 (1988).
15. Wishnow, E., Gush, H. & Ozier, I. Far-infrared spectrum of  $\text{N}_2$  and  $\text{N}_2$ -noble gas mixtures near 80 K. *J. Chem. Phys.* **104**, 3511–3516 (1996).
16. Lafferty, W. J., Solodov, A. M., Weber, A., Olson, W. B. & Hartmann, J.-M. Infrared collision-induced absorption by  $\text{N}_2$  near 43  $\mu\text{m}$  for atmospheric applications: measurements and empirical modeling. *Appl. Opt.* **35**, 5911 (1996).
17. Baranov, Y. I., Lafferty, W. J. & Fraser, G. T. Investigation of collision-induced absorption in the vibrational fundamental bands of  $\text{O}_2$  and  $\text{N}_2$  at elevated temperatures. *J. Mol. Spectrosc.* **233**, 160–163 (2005).
18. Hartmann, J.-M., Boulet, C. & Robert, D. *Collisional Effects on Molecular Spectra: Laboratory Experiments and Models, Consequences for Applications* (Elsevier, 2008).
19. de Kok, R., Irwin, P. G. J. & Teanby, N. A. Far-infrared opacity sources in Titan’s troposphere reconsidered. *Icarus* **209**, 854–857 (2010).
20. Höpfner, M., Milz, M., Buehler, S., Orphal, J. & Stiller, G. The natural greenhouse effect of atmospheric oxygen ( $\text{O}_2$ ) and nitrogen ( $\text{N}_2$ ). *Geophys. Res. Lett.* **39**, L10706 (2012).
21. Sung, K. et al. Progress in the measurement of temperature-dependent  $\text{N}_2\text{--N}_2$  collision-induced absorption and  $\text{H}_2$ -broadening

of cold and hot CH<sub>4</sub>. In *AAS/Division for Planetary Sciences Meeting Abstracts*# 48, **48**, 424–11 (2016).

22. Karman, T. et al. Update of the HITRAN collision-induced absorption section. *Icarus* **328**, 160–175 (2019).

23. Chistikov, D. N., Finenko, A. A., Lokshtanov, S. E., Petrov, S. V. & Vigasin, A. A. Simulation of collision-induced absorption spectra based on classical trajectories and ab initio potential and induced dipole surfaces. I. Case study of N<sub>2</sub>–N<sub>2</sub> rototranslational band. *J. Chem. Phys.* **151**, 194106 (2019).

24. Johnson, R., Bernath, P., Billinghamurst, B. & Zhao, J. Collision induced absorption spectra of N<sub>2</sub> and CH<sub>4</sub>. *J. Quant. Spectrosc. Rad. Transf.* **329**, 109189 (2024).

25. Dore, P. & Filabozzi, A. On the nitrogen-induced far-infrared absorption spectra. *Can. J. Phys.* **65**, 90–93 (1987).

26. Bussery-Honvault, B. & Hartmann, J.-M. Ab initio calculations for the far infrared collision induced absorption by N<sub>2</sub> gas. *J. Chem. Phys.* **140**, 054309 (2014).

27. Karman, T., Miliordos, E., Hunt, K. L., Groenenboom, G. C. & van der Avoird, A. Quantum mechanical calculation of the collision-induced absorption spectra of N<sub>2</sub>–N<sub>2</sub> with anisotropic interactions. *J. Chem. Phys.* **142**, 084306 (2015).

28. Hartmann, J.-M., Boulet, C. & Toon, G. Collision-induced absorption by N<sub>2</sub> near 2.16  $\mu$ m: Calculations, model, and consequences for atmospheric remote sensing. *J. Geophys. Res.: Atmos.* **122**, 2419–2428 (2017).

29. von Paris, P., Grenfell, J., Rauer, H. & Stock, J. N<sub>2</sub>-associated surface warming on early Mars. *Planet. Space Sci.* **82–83**, 149–154 (2013).

30. Rothman, L. et al. The HITRAN 2012 molecular spectroscopic database. *J. Quant. Spectrosc. Rad. Transf.* **130**, 4–50 (2013).

31. Gordon, I. E. et al. The HITRAN 2020 molecular spectroscopic database. *J. Quant. Spectrosc. Rad. Transf.* **276**, 107949 (2022).

32. Zhang, D. H., Wu, Q., Zhang, J. Z. H., von Dirke, M. & Baćić, Z. Exact full-dimensional bound state calculations for (HF)<sub>2</sub>, (DF)<sub>2</sub>, and HFDF. *J. Chem. Phys.* **102**, 2315–2325 (1995).

33. Császár, A. G., Allen, W. D., Yamaguchi, Y. & Schaefer III, H. F. Ab initio determination of accurate ground electronic state potential energy hypersurfaces for small molecules. In Jensen, P. & Bunker, P. R. (eds.) *Computational Molecular Spectroscopy*, pp. 15–68 (Wiley, 2000).

34. Bukowski, R., Szalewicz, K., Groenenboom, G. C. & Van der Avoird, A. Predictions of the properties of water from first principles. *Science* **315**, 1249–1252 (2007).

35. Metz, M. P., Piszczatowski, K. & Szalewicz, K. Automatic generation of intermolecular potential energy surfaces. *J. Chem. Theor. Comput.* **12**, 5895–5919 (2016).

36. Kodrycka, M. & Patkowski, K. Platinum, gold, and silver standards of intermolecular interaction energy calculations. *J. Chem. Phys.* **151**, 070901 (2019).

37. Simkó, I., Szidárovszky, T. & Császár, A. G. Toward automated variational computation of rovibrational resonances, including a case study of the H<sub>2</sub> dimer. *J. Chem. Theor. Comput.* **15**, 4156–4169 (2019).

38. Felker, P. M. & Baćić, Z. H<sub>2</sub>O–CO and D<sub>2</sub>O–CO complexes: Intra-and intermolecular rovibrational states from full-dimensional and fully coupled quantum calculations. *J. Chem. Phys.* **153**, 074107 (2020).

39. Metz, M. P. & Szalewicz, K. Automatic generation of flexible-monomer intermolecular potential energy surfaces. *J. Chem. Theor. Comput.* **16**, 2317–2339 (2020).

40. Felker, P. M. & Baćić, Z. Intra-and intermolecular rovibrational states of HCl–H<sub>2</sub>O and DCI–H<sub>2</sub>O dimers from full-dimensional and fully coupled quantum calculations. *Chin. J. Chem. Phys.* **34**, 728–740 (2021).

41. Felker, P. M., Liu, Y., Li, J. & Baćić, Z. DCI–H<sub>2</sub>O, HCl–D<sub>2</sub>O, and DCI–D<sub>2</sub>O dimers: Inter-and intramolecular vibrational states and frequency shifts from fully coupled quantum calculations on a full-dimensional neural network potential energy surface. *J. Phys. Chem. A* **125**, 6437–6449 (2021).

42. Felker, P. M. & Baćić, Z. Noncovalently bound molecular complexes beyond diatom–diatom systems: full-dimensional, fully coupled quantum calculations of rovibrational states. *Phys. Chem. Chem. Phys.* **24**, 24655–24676 (2022).

43. Jing, A., Szalewicz, K. & van der Avoird, A. Ammonia dimer: extremely fluxional but still hydrogen bonded. *Nat. Commun.* **13**, 1470 (2022).

44. Felker, P. M. & Baćić, Z. HF trimer: 12D fully coupled quantum calculations of HF-stretch excited intramolecular and intermolecular vibrational states using contracted bases of intramolecular and intermolecular eigenstates. *J. Chem. Phys.* **158**, 234109 (2023).

45. Raghavachari, K., Trucks, G. W., Pople, J. A. & Head-Gordon, M. A fifth-order perturbation comparison of electron correlation theories. *Chem. Phys. Lett.* **157**, 479–483 (1989).

46. Halkier, A. et al. Basis-set convergence in correlated calculations on Ne, N<sub>2</sub>, and H<sub>2</sub>O. *Chem. Phys. Lett.* **286**, 243–252 (1998).

47. Tasi, G. & Császár, A. G. Hartree–Fock-limit energies and structures with a few dozen distributed Gaussians. *Chem. Phys. Lett.* **438**, 139–143 (2007).

48. Boys, S. F. & Bernardi, F. The calculation of small molecular interactions by the differences of separate total energies. Some procedures with reduced errors. *Mol. Phys.* **19**, 553–566 (1970).

49. Császár, A. G., Allen, W. D. & Schaefer III, H. F. In pursuit of the ab initio limit for conformational energy prototypes. *J. Chem. Phys.* **108**, 9751–9764 (1998).

50. Tarczay, G., Császár, A. G., Klopper, W. & Quiney, H. M. Anatomy of relativistic energy corrections in light molecular systems. *Mol. Phys.* **99**, 1769–1794 (2001).

51. Allen, W. D., East, A. L. L. & Császár, A. G. Ab initio anharmonic vibrational analyses of non-rigid molecules. In Laane, J., Dakkouri, M., van der Veken, B. & Oberhammer, H. (eds.) *Structures and Conformations of Nonrigid Molecules*, pp. 343–373 (Kluwer, 1993).

52. Chung, H.-K. et al. Uncertainty estimates for theoretical atomic and molecular data. *J. Phys. D: Appl. Phys.* **49**, 363002 (2016).

53. Császár, A. G. et al. Dream or reality: complete basis set full configuration interaction potential energy hypersurfaces. In Demaison, J., Sarka, K. & Cohen, E. A. (eds.) *Spectroscopy from Space*, pp. 317–339 (Kluwer, 2001).

54. Szalewicz, K. & Jeziorski, B. Symmetry-adapted double-perturbation analysis of intramolecular correlation effects in weak intermolecular interactions: the He–He interaction. *Mol. Phys.* **38**, 191–208 (1979).

55. Rybak, S., Jeziorski, B. & Szalewicz, K. Many-body symmetry-adapted perturbation theory of intermolecular interactions. H<sub>2</sub>O and HF dimers. *J. Chem. Phys.* **95**, 6576–6601 (1991).

56. Szalewicz, K. Symmetry-adapted perturbation theory of intermolecular forces. *WIREs Comput. Mol. Sci.* **2**, 254–272 (2012).

57. Patkowski, K. Recent developments in symmetry-adapted perturbation theory. *WIREs Comput. Mol. Sci.* **10**, e1452 (2020).

58. Garcia, J., Podeszwa, R. & Szalewicz, K. SAPT codes for calculations of intermolecular interaction energies. *J. Chem. Phys.* **152**, 184109 (2020).

59. Berns, R. M. & van der Avoird, A. N<sub>2</sub>–N<sub>2</sub> interaction potential from ab initio calculations, with application to the structure of (N<sub>2</sub>)<sub>2</sub>. *J. Chem. Phys.* **72**, 6107–6116 (1980).

60. Jönsson, B., Karlström, G. & Romano, S. Monte Carlo simulations of liquid and solid nitrogen based on an ab initio MO–LCAO–SCF–CI potential. *J. Chem. Phys.* **74**, 2896–2903 (1981).

61. Ling, M. S. H. & Rigby, M. Toward an intermolecular potential for nitrogen. *Mol. Phys.* **51**, 855 (1984).

62. Böhm, H.-J. & Ahlrichs, R. The N<sub>2</sub>–N<sub>2</sub> interaction: a theoretical investigation. *Mol. Phys.* **55**, 1159–1169 (1985).

63. LeSar, R. & Shaw, M. An electron–gas plus damped-dispersion calculation of the N<sub>2</sub>–N<sub>2</sub> interaction. *J. Chem. Phys.* **84**, 5479–5485 (1986).

64. van der Avoird, A., Wormer, P. E. S. & Jansen, A. P. J. An improved intermolecular potential for nitrogen. *J. Chem. Phys.* **84**, 1629–1635 (1986).

65. Stallcop, J. R. & Partridge, H. The N<sub>2</sub>–N<sub>2</sub> potential energy surface. *Chem. Phys. Lett.* **281**, 212–220 (1997).

66. Aquilanti, V., Bartolomei, M., Cappelletti, D., Carmona-Novillo, E. & Pirani, F. The N<sub>2</sub>–N<sub>2</sub> system: an experimental potential energy surface and calculated rotovibrational levels of the molecular nitrogen dimer. *J. Chem. Phys.* **117**, 615–627 (2002).

67. Leonhard, K. & Deiters, U. K. Monte Carlo simulations of nitrogen using an ab initio potential. *Mol. Phys.* **100**, 2571–2585 (2002).

68. Karimi-Jafari, M. H., Maghari, A. & Shahbazian, S. An improved ab initio potential energy surface for N<sub>2</sub>–N<sub>2</sub>. *Chem. Phys.* **314**, 249–262 (2005).

69. Gomez, L. et al. Global fits of new intermolecular ground state potential energy surfaces for N<sub>2</sub>–H<sub>2</sub> and N<sub>2</sub>–N<sub>2</sub> van der Waals dimers. *Chem. Phys. Lett.* **445**, 99–107 (2007).

70. Strąk, P. & Krukowski, S. Molecular nitrogen–N<sub>2</sub> properties: the intermolecular potential and the equation of state. *J. Chem. Phys.* **126**, 194501 (2007).

71. Cappelletti, D., Pirani, F., Bussery-Honvaut, B., Gomez, L. & Bartolomei, M. A bond–bond description of the intermolecular interaction energy: the case of weakly bound N<sub>2</sub>–H<sub>2</sub> and N<sub>2</sub>–N<sub>2</sub> complexes. *Phys. Chem. Chem. Phys.* **10**, 4281–4293 (2008).

72. Hellmann, R. Ab initio potential energy surface for the nitrogen molecule pair and thermophysical properties of nitrogen gas. *Mol. Phys.* **111**, 387–401 (2013).

73. Pacifici, L., Verdicchio, M., Lago, N. F., Lombardi, A. & Costantini, A. A high-level ab initio study of the N<sub>2</sub> + N<sub>2</sub> reaction channel. *J. Comput. Chem.* **34**, 2668–2676 (2013).

74. Paukku, Y., Yang, K. R., Varga, Z. & Truhlar, D. G. Global ab initio ground-state potential energy surface of N<sub>4</sub>. *J. Chem. Phys.* **139**, 044309 (2013).

75. Li, J., Varga, Z., Truhlar, D. G. & Guo, H. Many-body permutationally invariant polynomial neural network potential energy surface for N<sub>4</sub>. *J. Chem. Theor. Comput.* **16**, 4822–4832 (2020).

76. Karimi-Jafari, M. H. & Ashouri, M. Quantifying the anisotropy of intermolecular potential energy surfaces: a critical assessment of available N<sub>2</sub>–N<sub>2</sub> potentials. *Phys. Chem. Chem. Phys.* **13**, 9887–9894 (2011).

77. Tennyson, J. & van der Avoird, A. Quantum dynamics of the van der Waals molecule (N<sub>2</sub>)<sub>2</sub>: An ab initio treatment. *J. Chem. Phys.* **77**, 5664–5681 (1982).

78. Brocks, G. & van der Avoird, A. Infrared spectra of the van der Waals molecule (N<sub>2</sub>)<sub>2</sub>. *Mol. Phys.* **55**, 11–32 (1985).

79. Bunker, P. R. & Jensen, P. *Molecular Symmetry and Spectroscopy* (NRC Research Press, 2006).

80. Császár, A. G., Fábri, C. & Sarka, J. Quasistructural molecules. *WIREs Comput. Mol. Sci.* **10**, e1432 (2020).

81. Császár, A. G. et al. The fourth age of quantum chemistry: molecules in motion. *Phys. Chem. Chem. Phys.* **14**, 1085–1106 (2012).

82. Császár, A. G. et al. Rotational–vibrational resonance states. *Phys. Chem. Chem. Phys.* **22**, 15081–15104 (2020).

83. Tóbiás, R., Simkó, I. & Császár, A. G. Unusual dynamics and vibrational fingerprints of van der Waals dimers formed by linear molecules and rare-gas atoms. *J. Chem. Theor. Comput.* **19**, 8767–8781 (2023).

84. Smith, D. G. A., Jankowski, P., Slawik, M., Witek, H. A. & Patkowski, K. Basis set convergence of the post-CCSD(T) contribution to noncovalent interaction energies. *J. Chem. Theory Comput.* **10**, 3140–3150 (2014).

85. Dunning Jr, T. H. Gaussian basis sets for use in correlated molecular calculations. I. The atoms boron through neon and hydrogen. *J. Chem. Phys.* **90**, 1007–1023 (1989).

86. Tóbiás, R. et al. Separate supplementary files to the paper “Rovibrational dynamics of the quasistructural N<sub>2</sub> dimer”. <https://doi.org/10.17605/OSF.IO/RJ6XB>

87. McKee, M. L. Fluctional molecules. *WIREs Comput. Mol. Sci.* **1**, 943–951 (2011).

88. Fábri, C., Császár, A. G. & Czakó, G. Reduced-dimensional quantum computations for the rotational–vibrational dynamics of F<sup>–</sup>–CH<sub>4</sub> and F<sup>–</sup>–CH<sub>2</sub>D<sub>2</sub>. *J. Chem. Phys.* **117**, 6975–6983 (2003).

89. Fábri, C., Sarka, J. & Császár, A. G. Communication: rigidity of the molecular ion H<sub>5</sub><sup>+</sup>. *J. Chem. Phys.* **140**, 051101 (2014).

90. Sarka, J. et al. Modelling rotations, vibrations, and rovibrational couplings in astructural molecules – a case study based on the H<sub>5</sub><sup>+</sup> molecular ion. *Mol. Phys.* **113**, 1873–1883 (2015).

91. Sarka, J. & Császár, A. G. Interpretation of the vibrational energy level structure of the astructural molecular ion H<sub>5</sub><sup>+</sup> and all of its deuterated isotopomers. *J. Chem. Phys.* **144**, 154309 (2016).

92. Fábri, C., Quack, M. & Császár, A. G. On the use of nonrigid-molecular symmetry in nuclear-motion computations employing a discrete variable representation: a case study of the bending energy levels of CH<sub>5</sub><sup>+</sup>. *J. Chem. Phys.* **147**, 134101 (2017).

93. Rawlinson, J. I. Quantum graph model for rovibrational states of protonated methane. *J. Chem. Phys.* **151**, 164303 (2019).

94. Metz, M. P. et al. Molecular dimers of methane clathrates: ab initio potential energy surfaces and variational vibrational states. *Phys. Chem. Chem. Phys.* **21**, 13504–13525 (2019).

95. Mátyus, E. et al. Assigning quantum labels to variationally computed rotational–vibrational eigenstates of polyatomic molecules. *J. Chem. Phys.* **133**, 034113 (2010).

96. Walsh, M., England, T., Dyke, T. & Howard, B. Pulsed molecular beam infrared absorption spectroscopy of CO<sub>2</sub> dimer. *Chem. Phys. Lett.* **142**, 265–270 (1987).

97. Rezaei, M., Sheybani-Deloui, S., Moazzen-Ahmadi, N., Michaelian, K. & McKellar, A. CO dimer: The infrared spectrum revisited. *J. Phys. Chem. A* **117**, 9612–9620 (2013).

98. Tóbiás, R., Furtenbacher, T. & Császár, A. G. Past, present, and future of joint utilization of experimental, empirical, and computed spectroscopic data: Challenges, advantages, and recommendations. *Adv. Quant. Chem.*, **93** <https://doi.org/10.1016/bs.aqc.2025.01.002> (2025).

99. Wilson Jr, E. B., Decius, J. C. & Cross, P. C. *Molecular Vibrations: The Theory of Infrared and Raman Vibrational Spectra* (McGraw Hill, 1955).

100. Essén, H. & Svensson, M. Calculation of coordinates from molecular geometric parameters and the concept of a geometric calculator. *Comp. Chem.* **20**, 389–395 (1996).

101. Kendall, R. A., Dunning Jr, T. H. & Harrison, R. J. Electron affinities of the 1st-row atoms revisited – Systematic basis sets and wave functions. *J. Chem. Phys.* **96**, 6796–6806 (1992).

102. Misquitta, A. J., Jeziorski, B. & Szalewicz, K. Dispersion energy from density-functional theory description of monomers. *Phys. Rev. Lett.* **91**, 033201 (2003).

103. Bukowski, R., Podeszwa, R. & Szalewicz, K. Efficient calculation of coupled Kohn–Sham dynamic susceptibility functions and dispersion energies with density fitting. *Chem. Phys. Lett.* **414**, 111–116 (2005).

104. Podeszwa, R., Bukowski, R. & Szalewicz, K. Density-fitting method in symmetry-adapted perturbation theory based on kohn–sham description of monomers. *J. Chem. Theor. Comput.* **2**, 400–412 (2006).

105. Adamo, C. & Barone, V. Toward reliable density functional methods without adjustable parameters: The PBE0 model. *J. Chem. Phys.* **110**, 6158–6170 (1999).

106. Akin-Ojo, O., Bukowski, R. & Szalewicz, K. Ab initio studies of He-HCCN interaction. *J. Chem. Phys.* **119**, 8379–8396 (2003).
107. Helgaker, T., Klopper, W., Koch, H. & Noga, J. Basis-set convergence of correlated calculations on water. *J. Chem. Phys.* **106**, 9639–9646 (1997).
108. MOLPRO website, last accessed on September 1, 2025. <https://www.molpro.net/>
109. Neese, F., Wennmohs, F., Becker, U. & Riplinger, C. The ORCA quantum chemistry program package. *J. Chem. Phys.* **152**, 224108 (2020).
110. Bendtsen, J. The rotational and rotation-vibrational Raman spectra of  $^{14}\text{N}_2$ ,  $^{14}\text{N}^{15}\text{N}$  and  $^{15}\text{N}_2$ . *J. Raman. Spectrosc.* **2**, 133–145 (1974).
111. Jeziorski, B., Moszynski, R. & Szalewicz, K. Perturbation theory approach to intermolecular potential energy surfaces of van der Waals complexes. *Chem. Rev.* **94**, 1887–1930 (1994).
112. Sparta, M., Toffoli, D. & Christiansen, O. An adaptive density-guided approach for the generation of potential energy surfaces of polyatomic molecules. *Theor. Chem. Acc.* **123**, 413–429 (2009).
113. Bunker, P. R. Symmetry in  $(\text{H}_2)_2$ ,  $(\text{D}_2)_2$ , and  $\text{H}_2\text{D}_2$  Van der Waals complexes. *Can. J. Phys.* **57**, 2099–2105 (1979).
114. Merer, A. & Watson, J. K. Symmetry considerations for internal rotation in ethylene-like molecules. *J. Mol. Spec.* **47**, 499–514 (1973).
115. Mátyus, E., Czakó, G. & Császár, A. G. Toward black-box-type full- and reduced-dimensional variational (ro)vibrational computations. *J. Chem. Phys.* **130**, 134112 (2009).
116. Fábris, C., Mátyus, E. & Császár, A. G. Rotating full- and reduced-dimensional quantum chemical models of molecules. *J. Chem. Phys.* **134**, 074105 (2011).
117. Schiffel, G. & Manthe, U. On direct product based discrete variable representations for angular coordinates and the treatment of singular terms in the kinetic energy operator. *Chem. Phys.* **374**, 118–125 (2010).
118. Wang, X.-G. & Carrington Jr, T.  $K$ -independent vibrational bases for systems with large amplitude motion. *Mol. Phys.* **110**, 825–835 (2012).
119. Avila, G. & Mátyus, E. Toward breaking the curse of dimensionality in (ro)vibrational computations of molecular systems with multiple large-amplitude motions. *J. Chem. Phys.* **150**, 174107 (2019).
120. Watson, J. K. G. Determination of centrifugal distortion coefficients of asymmetric-top molecules. *J. Chem. Phys.* **46**, 1935–1948 (1967).
121. Echave, J. & Clary, D. C. Potential optimized discrete variable representation. *Chem. Phys. Lett.* **190**, 225–230 (1992).
122. Szalay, V. Discrete variable representations of differential operators. *J. Chem. Phys.* **99**, 1978–1984 (1993).
123. Meyer, R. Trigonometric interpolation method for one-dimensional quantum-mechanical problems. *J. Chem. Phys.* **52**, 2053–2059 (1970).
124. Wu, K. & Simon, H. D. Thick-restart Lanczos method for large symmetric eigenvalue problems. *SIAM J. Matrix Anal. A.* **22**, 602–616 (2000).
125. Dax, A. A compact Heart iteration for large eigenvalues problems. *Adv. Linear Algebra Matrix Theory* **12**, 24–38 (2022).

## Acknowledgements

This project received funding from the National Research, Development, and Innovation Office of Hungary (NKFIH, grant no. K138233 to AGC and PD145972 to RT). The research was also supported by the János Bolyai Research Scholarship of the Hungarian Academy of Sciences (given to CF). The work performed in Auburn received support from the U.S. National Science Foundation CAREER award CHE-1351978. This publication supports research conducted within the COST Action CA21101 “Confined molecular systems: from a new generation of materials to the stars” (COSY), funded by the European Cooperation in Science and Technology (COST)

and the MSCA Doctoral Network PHYMOL, “Physics, Accuracy and Machine Learning: Towards the Next Generation of Molecular Potentials.” The authors thank Dr. Robert Hellmann for providing a FORTRAN code which enabled the evaluation of the N2d-HOB potential, as well as for allowing its inclusion in their OSF repository<sup>86</sup>. AGC appreciates discussions with Dr. Tijs Karman about the CIA spectrum of the nitrogen gas, while RT is grateful to Dr. Irén Simkó and Dr. János Sarka for useful comments.

## Author contributions

Roland Tóbiás: Conceptualization (equal); Data curation (lead); Formal analysis (lead); Investigation (equal); Methodology (lead); Software (lead); Supervision (equal); Validation (equal); Visualization (lead); Writing—original draft (equal); Writing—review and editing (equal). Csaba Fábris: Formal analysis (supporting); Investigation (equal); Methodology (supporting); Validation (equal); Visualization (supporting); Writing—original draft (supporting); Writing—review and editing (equal). Marlene Bosquez: Data curation (supporting); Investigation (supporting); Visualization (supporting); Project administration (equal); Validation (supporting); Writing—review and editing (supporting). Monika Kodrycka: Data curation (supporting); Writing—review and editing (supporting). Konrad Patkowski: Data curation (supporting); Writing—review and editing (supporting). Attila G. Császár: Conceptualization (equal); Funding acquisition (lead); Investigation (supporting); Methodology (supporting); Project administration (equal); Resources (equal); Supervision (equal); Validation (equal); Writing—original draft (equal); Writing—review & editing (equal).

## Competing interests

The authors declare no competing interests.

## Additional information

**Supplementary information** The online version contains supplementary material available at <https://doi.org/10.1038/s42004-025-01716-7>.

**Correspondence** and requests for materials should be addressed to Roland Tóbiás or Attila G. Császár.

**Peer review information** *Communications Chemistry* thanks Xiao-Gang Wang, Andrey Yachmenev, and the other anonymous reviewer for their contribution to the peer review of this work.

**Reprints and permissions information** is available at <http://www.nature.com/reprints>

**Publisher's note** Springer Nature remains neutral with regard to jurisdictional claims in published maps and institutional affiliations.

**Open Access** This article is licensed under a Creative Commons Attribution 4.0 International License, which permits use, sharing, adaptation, distribution and reproduction in any medium or format, as long as you give appropriate credit to the original author(s) and the source, provide a link to the Creative Commons licence, and indicate if changes were made. The images or other third party material in this article are included in the article's Creative Commons licence, unless indicated otherwise in a credit line to the material. If material is not included in the article's Creative Commons licence and your intended use is not permitted by statutory regulation or exceeds the permitted use, you will need to obtain permission directly from the copyright holder. To view a copy of this licence, visit <http://creativecommons.org/licenses/by/4.0/>.

© The Author(s) 2025